GeV OBSERVATIONS OF STAR-FORMING GALAXIES WITH THE *FERMI* LARGE AREA TELESCOPE

M. ACKERMANN[1], M. AJELLO[2], A. ALLAFORT[2], L. BALDINI[3], J. BALLET[4], D. BASTIERI[5,6], K. BECHTOL[2], R. BELLAZZINI[3], B. BERENJI[2], E. D. BLOOM[2], E. BONAMENTE[7,8], A. W. BORGLAND[2], A. BOUVIER[9], J. BREGEON[3], M. BRIGIDA[10,11], P. BRUEL[12], R. BUEHLER[2], S. BUSON[5,6], G. A. CALIANDRO[13], R. A. CAMERON[2], P. A. CARAVEO[14], J. M. CASANDJIAN[4], C. CECCHI[7,8], E. CHARLES[2], A. CHEKHTMAN[15,51], C. C. CHEUNG[16,51], J. CHIANG[2], A. N. CILLIS[17,18], S. CIPRINI[8,19], R. CLAUS[2], J. COHEN-TANUGI[20], J. CONRAD[21,22,52], S. CUTINI[19], F. DE PALMA[10,11], C. D. DERMER[23], S. W. DIGEL[2], E. DO COUTO E SILVA[2], P. S. DRELL[2], A. DRLICA-WAGNER[2], C. FAVUZZI[10,11], S. J. FEGAN[12], P. FORTIN[12], Y. FUKAZAWA[24], S. FUNK[2], P. FUSCO[10,11], F. GARGANO[11], D. GASPARRINI[19], S. GERMANI[7,8], N. GIGLIETTO[10,11], F. GIORDANO[10,11], T. GLANZMAN[2], G. GODFREY[2], I. A. GRENIER[4], S. GUIREC[25], M. GUSTAFSSON[5], D. HADASCH[13], M. HAYASHIDA[2,26], E. HAYS[18], R. E. HUGHES[27], G. JÓHANNESSON[28], A. S. JOHNSON[2], T. KAMAE[2], H. KATAGIRI[29], J. KATAOKA[30], J. KNÖDLSEDER[31,32], M. KUSS[3], J. LANDE[2], F. LONGO[33,34], F. LOPARCO[10,11], B. LOTT[35], M. N. LOVELLETTE[23], P. LUBRANO[7,8], G. M. MADEJSKI[2], P. MARTIN[36], M. N. MAZZIOTTA[11], J. E. MCENERY[18,37], P. F. MICHELSON[2], T. MIZUNO[38], C. MONTE[10,11], M. E. MONZANI[2], A. MORSELLI[39], I. V. MOSKALENKO[2], S. MURGIA[2], S. NISHINO[24], J. P. NORRIS[40], E. NUSS[20], M. OHNO[41], T. OHSUGI[38], A. OKUMURA[2,42], N. OMODEI[2], E. ORLANDO[2], M. OZAKI[41], D. PARENT[15,51], M. PERSIC[33,43], M. PESCE-ROLLINS[3], V. PETROSIAN[2], M. PIERBATTISTA[4], F. PIRON[20], G. PIVATO[6], T. A. PORTER[2], S. RAINÒ[10,11], R. RANDO[5,6], M. RAZZANO[3,9], A. REIMER[2,44], O. REIMER[2,44], S. RITZ[9], M. ROTH[45], C. SBARRA[5], C. SGRÒ[3], E. J. SISKIND[46], G. SPANDRE[3], P. SPINELLI[10,11], ŁUKASZ STAWARZ[41,47], A. W. STRONG[36], H. TAKAHASHI[24], T. TANAKA[2], J. B. THAYER[2], L. TIBALDO[5,6], M. TINIVELLA[3], D. F. TORRES[13,48], G. TOSTI[7,8], E. TROJA[18,53], Y. UCHIYAMA[2], J. VANDENBROUCKE[2], G. VIANELLO[2,49], V. VITALE[39,50], A. P. WAITE[2], M. WOOD[2], AND Z. YANG[21,22]

[1] Deutsches Elektronen Synchrotron DESY, D-15738 Zeuthen, Germany
[2] W. W. Hansen Experimental Physics Laboratory, Kavli Institute for Particle Astrophysics and Cosmology, Department of Physics and SLAC National Accelerator Laboratory, Stanford University, Stanford, CA 94305, USA; bechtol@stanford.edu, funk@slac.stanford.edu
[3] Istituto Nazionale di Fisica Nucleare, Sezione di Pisa, I-56127 Pisa, Italy
[4] Laboratoire AIM, CEA-IRFU/CNRS/Université Paris Diderot, Service d'Astrophysique, CEA Saclay, F-91191 Gif sur Yvette, France
[5] Istituto Nazionale di Fisica Nucleare, Sezione di Padova, I-35131 Padova, Italy
[6] Dipartimento di Fisica "G. Galilei," Università di Padova, I-35131 Padova, Italy
[7] Istituto Nazionale di Fisica Nucleare, Sezione di Perugia, I-06123 Perugia, Italy
[8] Dipartimento di Fisica, Università degli Studi di Perugia, I-06123 Perugia, Italy
[9] Santa Cruz Institute for Particle Physics, Department of Physics and Department of Astronomy and Astrophysics, University of California at Santa Cruz, Santa Cruz, CA 95064, USA
[10] Dipartimento di Fisica "M. Merlin" dell'Università e del Politecnico di Bari, I-70126 Bari, Italy
[11] Istituto Nazionale di Fisica Nucleare, Sezione di Bari, I-70126 Bari, Italy
[12] Laboratoire Leprince-Ringuet, École polytechnique, CNRS/IN2P3, Palaiseau, France
[13] Institut de Ciències de l'Espai (IEEE-CSIC), Campus UAB, 08193 Barcelona, Spain; dtorres@ieec.uab.es
[14] INAF-Istituto di Astrofisica Spaziale e Fisica Cosmica, I-20133 Milano, Italy
[15] Center for Earth Observing and Space Research, College of Science, George Mason University, Fairfax, VA 22030, USA
[16] National Research Council Research Associate, National Academy of Sciences, Washington, DC 20001, USA
[17] Instituto de Astronomía y Fisica del Espacio, Parbellón IAFE, Cdad. Universitaria, Buenos Aires, Argentina; analia.cillis@gmail.com
[18] NASA Goddard Space Flight Center, Greenbelt, MD 20771, USA
[19] Agenzia Spaziale Italiana (ASI) Science Data Center, I-00044 Frascati (Roma), Italy
[20] Laboratoire Univers et Particules de Montpellier, Université Montpellier 2, CNRS/IN2P3, Montpellier, France
[21] Department of Physics, Stockholm University, AlbaNova, SE-106 91 Stockholm, Sweden
[22] The Oskar Klein Centre for Cosmoparticle Physics, AlbaNova, SE-106 91 Stockholm, Sweden
[23] Space Science Division, Naval Research Laboratory, Washington, DC 20375-5352, USA
[24] Department of Physical Sciences, Hiroshima University, Higashi-Hiroshima, Hiroshima 739-8526, Japan
[25] Center for Space Plasma and Aeronomic Research (CSPAR), University of Alabama in Huntsville, Huntsville, AL 35899, USA
[26] Department of Astronomy, Graduate School of Science, Kyoto University, Sakyo-ku, Kyoto 606-8502, Japan
[27] Department of Physics, Center for Cosmology and Astro-Particle Physics, The Ohio State University, Columbus, OH 43210, USA
[28] Science Institute, University of Iceland, IS-107 Reykjavik, Iceland
[29] College of Science, Ibaraki University, 2-1-1 Bunkyo, Mito 310-8512, Japan
[30] Research Institute for Science and Engineering, Waseda University, 3-4-1 Okubo, Shinjuku, Tokyo 169-8555, Japan
[31] CNRS, IRAP, F-31028 Toulouse cedex 4, France
[32] GAHEC, Université de Toulouse, UPS-OMP, IRAP, Toulouse, France
[33] Istituto Nazionale di Fisica Nucleare, Sezione di Trieste, I-34127 Trieste, Italy
[34] Dipartimento di Fisica, Università di Trieste, I-34127 Trieste, Italy
[35] Université Bordeaux 1, CNRS/IN2p3, Centre d'Études Nucléaires de Bordeaux Gradignan, F-33175 Gradignan, France
[36] Max-Planck Institut für extraterrestrische Physik, D-85748 Garching, Germany
[37] Department of Physics and Department of Astronomy, University of Maryland, College Park, MD 20742, USA
[38] Hiroshima Astrophysical Science Center, Hiroshima University, Higashi-Hiroshima, Hiroshima 739-8526, Japan
[39] Istituto Nazionale di Fisica Nucleare, Sezione di Roma "Tor Vergata," I-00133 Roma, Italy
[40] Department of Physics, Boise State University, Boise, ID 83725, USA
[41] Institute of Space and Astronautical Science, JAXA, 3-1-1 Yoshinodai, Chuo-ku, Sagamihara, Kanagawa 252-5210, Japan
[42] Solar-Terrestrial Environment Laboratory, Nagoya University, Nagoya 464-8601, Japan
[43] Osservatorio Astronomico di Trieste, Istituto Nazionale di Astrofisica, I-34143 Trieste, Italy
[44] Institut für Astro- und Teilchenphysik and Institut für Theoretische Physik, Leopold-Franzens-Universität Innsbruck, A-6020 Innsbruck, Austria
[45] Department of Physics, University of Washington, Seattle, WA 98195-1560, USA
[46] NYCB Real-Time Computing Inc., Lattingtown, NY 11560-1025, USA
[47] Astronomical Observatory, Jagiellonian University, 30-244 Kraków, Poland
[48] Institució Catalana de Recerca i Estudis Avançats (ICREA), Barcelona, Spain

[49] Consorzio Interuniversitario per la Fisica Spaziale (CIFS), I-10133 Torino, Italy
[50] Dipartimento di Fisica, Università di Roma "Tor Vergata," I-00133 Roma, Italy

ABSTRACT

Recent detections of the starburst galaxies M82 and NGC 253 by gamma-ray telescopes suggest that galaxies rapidly forming massive stars are more luminous at gamma-ray energies compared to their quiescent relatives. Building upon those results, we examine a sample of 69 dwarf, spiral, and luminous and ultraluminous infrared galaxies at photon energies 0.1–100 GeV using 3 years of data collected by the Large Area Telescope (LAT) on the *Fermi Gamma-ray Space Telescope* (*Fermi*). Measured fluxes from significantly detected sources and flux upper limits for the remaining galaxies are used to explore the physics of cosmic rays in galaxies. We find further evidence for quasi-linear scaling relations between gamma-ray luminosity and both radio continuum luminosity and total infrared luminosity which apply both to quiescent galaxies of the Local Group and low-redshift starburst galaxies (conservative P-values $\lesssim 0.05$ accounting for statistical and systematic uncertainties). The normalizations of these scaling relations correspond to luminosity ratios of $\log(L_{0.1-100\,\mathrm{GeV}}/L_{1.4\,\mathrm{GHz}}) = 1.7 \pm 0.1_{(\mathrm{statistical})} \pm 0.2_{(\mathrm{dispersion})}$ and $\log(L_{0.1-100\,\mathrm{GeV}}/L_{8-1000\,\mu\mathrm{m}}) = -4.3 \pm 0.1_{(\mathrm{statistical})} \pm 0.2_{(\mathrm{dispersion})}$ for a galaxy with a star formation rate of $1\,M_\odot\,\mathrm{yr}^{-1}$, assuming a Chabrier initial mass function. Using the relationship between infrared luminosity and gamma-ray luminosity, the collective intensity of unresolved star-forming galaxies at redshifts $0 < z < 2.5$ above 0.1 GeV is estimated to be 0.4–2.4 $\times 10^{-6}$ ph cm^{-2} s^{-1} sr^{-1} (4%–23% of the intensity of the isotropic diffuse component measured with the LAT). We anticipate that $\sim$10 galaxies could be detected by their cosmic-ray-induced gamma-ray emission during a 10 year *Fermi* mission.

Key words: cosmic rays – galaxies: starburst – gamma rays: diffuse background – gamma rays: galaxies

Online-only material: color figures

1. INTRODUCTION

Global emission of most galaxies across much of the electromagnetic spectrum from radio to gamma-ray energies is related to the formation and destruction of massive stars. The exceptions are certain galaxies hosting active galactic nuclei (AGNs). Throughout this work, we refer to galaxies in which non-thermal emission is mainly diffuse in origin rather than powered by a supermassive black hole as "star-forming galaxies."

O and B stars radiate the majority of their bolometric luminosity at ultraviolet wavelengths, which is efficiently absorbed by interstellar dust and re-emitted in the infrared (IR; Scoville & Young 1983). The IR emission dominates the spectral energy distribution of actively star-forming galaxies (reviewed by Sanders & Mirabel 1996) and is a robust indicator of star formation rates (SFRs; e.g., Kennicutt 1998a). Starburst galaxies are distinguished by kpc-scale regions of intense star-forming activity and are often identified by their enormous IR luminosities, many being classified as luminous infrared galaxies (LIRGs, $L_{8-1000\,\mu\mathrm{m}} > 10^{11}\,L_\odot$) and ultraluminous infrared galaxies (ULIRGs, $L_{8-1000\,\mu\mathrm{m}} > 10^{12}\,L_\odot$) using the definition proposed by Sanders & Mirabel (1996).

Massive stars responsible for the IR emission end their lives as core-collapse supernovae (SNe), whose remnants are believed to be the main cosmic-ray (CR, including all species) accelerators on galactic scales. The energy budget of CRs observed in the solar neighborhood is dominated by relativistic protons. If $\sim$10% of the mechanical energy of the outgoing shocks can be transferred into CR acceleration, supernova remnants (SNRs) would be capable of sustaining the locally measured CR flux (Ginzburg & Syrovatskii 1964).

In star-forming galaxies, CR electrons and positrons (hereafter simply electrons) spiraling in interstellar magnetic fields radiate diffuse synchrotron emission in the radio continuum (RC) at a level closely related to the total IR luminosity of the galaxies (van der Kruit 1971, 1973; de Jong et al. 1985; Helou et al. 1985; Condon 1992). Thermal bremsstrahlung emission originating from H II regions ionized by the massive stars contributes to the RC emission to a lesser extent. Remarkably, the nearly linear empirical RC–IR correlation spans over five orders of magnitude in luminosity (Condon et al. 1991).

CRs also create diffuse gamma-ray emission. The same CR electrons responsible for radio synchrotron emission can produce high-energy radiation either through interactions with gas (bremsstrahlung) or interstellar radiation fields (inverse Compton scattering). Inelastic collisions between CR nuclei and ambient gas lead to the production of gamma rays through π^0 decay, and also to the production of secondary CR leptons by $\pi^\pm$ decay. It is therefore natural to look for correlations of gamma rays with the CR-induced emissions at lower frequencies (and accordingly, IR emissions).

Two of the nearest starburst galaxies, M82 and NGC 253, have been detected in high-energy gamma rays by both space-based (Abdo et al. 2010d) and imaging air-Cerenkov telescopes (Acciari et al. 2009; Acero et al. 2009). Although all galaxies are expected to produce CR-induced emission at some level, large numbers of SNRs together with dense interstellar gas (average number densities $\sim$500 cm^{-3}) and intense radiation fields led several authors to anticipate the central starbursts of M82 and NGC 253 as detectable gamma-ray sources (e.g., Paglione et al. 1996; Blom et al. 1999; Domingo-Santamaría & Torres 2005; Persic et al. 2008; de Cea del Pozo et al. 2009; Rephaeli et al. 2010). Because the massive stars ($M \gtrsim 8\,M_\odot$) which ultimately result in core-collapse SNe have lifetimes of $\mathcal{O}(10^7$ yr), and particle acceleration in the vicinity of an SN happens for a short time $\mathcal{O}(10^4$ yr), the number of CR accelerators in a given galaxy is thought to be closely related to the contemporaneous SFR.

Indeed, the observed gamma-ray fluxes from M82 and NGC 253 imply enhanced CR energy densities within galaxies undergoing rapid massive star formation.

A study of the Local Group galaxies detected at GeV energies, including the Milky Way (MW), Small Magellanic Cloud (SMC; Abdo et al. 2010h) and Large Magellanic Cloud (LMC; Abdo et al. 2010e), and M31, identified a simple power-law relation between star formation and gamma-ray luminosity (Abdo et al. 2010b). On spatial scales within an individual galaxy, resolved images of the LMC at GeV energies show that gamma-ray emissivity per hydrogen atom, and hence CR intensity, is greatest near the massive star-forming region 30 Doradus (Abdo et al. 2010e).

EGRET observations (Cillis et al. 2005) yielded flux upper limits for a collection of star-forming galaxies beyond the Local Group (typical limits of $3–5 \times 10^{-8}$ ph cm^{-2} s^{-1} in the >0.1 GeV energy range), and stacking searches for a collective signal from the same galaxies produced no significant detection. Lenain & Walter (2011) recently reported flux upper limits in the 0.2–200 GeV energy range for several galaxies located within 5 Mpc including M81, M83, IC 342, Maffei 1, Maffei 2, and M94 using 29 months of data collected by the Large Area Telescope (LAT) on board the *Fermi Gamma-ray Space Telescope* (*Fermi*). The MAGIC Collaboration has reported a flux upper limit in the energy range $\gtrsim$160 GeV toward the nearest ULIRG, Arp 220 (15 hr; Albert et al. 2007), and H.E.S.S. observations of NGC 1068 produced a flux upper limit above 210 GeV (4.3 hr; Aharonian et al. 2005).

In this paper, we use 3 years of *Fermi*-LAT data to perform a systematic search for high-energy gamma-ray emission from 64 star-forming galaxies beyond the Local Group selected on the basis of their present star-forming activity. The next section describes our galaxy sample. Section 3 outlines our analysis of LAT data and we present results in Section 4, including updated spectral energy distributions for significantly detected galaxies and flux upper limits for the remaining candidates. Five Local Group galaxies previously studied in LAT data, the SMC, LMC, MW, M31, and M33, are additionally included in a population study of low-redshift star-forming galaxies. Our primary objective is to explore the global properties of galaxies related to their CR-induced emissions. We find that a simple power-law relationship between gamma-ray luminosity and SFR reported for Local Group galaxies (Abdo et al. 2010b) also describes the larger set of star-forming galaxies examined here. The implications of this scaling relation both for the physics of CRs and the contribution of non-AGN-dominated star-forming galaxies to the isotropic diffuse gamma-ray background (IGRB) are discussed in Section 5, and we predict which galaxies might be detected over the course of a 10 year *Fermi* mission. A standard ΛCDM cosmology with $\Omega_M = 0.3$, $\Omega_\Lambda = 0.7$, and $H_0 = 75$ km s^{-1} Mpc^{-1} is used throughout.

2. GALAXY SAMPLE

Massive star formation is fueled by the availability of dense molecular gas in the interstellar medium (ISM). In order to select a sample of galaxies with unambiguous ongoing star formation, we base our sample of galaxies on the HCN survey of Gao & Solomon (2004a). HCN $J = 1–0$ line emission is stimulated in the presence of dense molecular gas ($n_{H_2} > 3 \times 10^4$ cm^{-3}) typically associated with giant molecular clouds where the majority of star formation occurs (Solomon et al. 1979). The total quantity of molecular gas in the dense phase as measured by HCN-line emission exhibits a low-scatter linear correlation

with both total IR luminosity (Gao & Solomon 2004b) and RC luminosity (Liu & Gao 2010) and is considered a reliable indicator of SFR. Observations of Galactic molecular clouds suggest that these relations hold at the scale of individual molecular cloud cores as well (Wu et al. 2005).

The HCN survey is the most complete study to date in terms of total dense molecular gas content, including nearly all of the nearby IR-bright galaxies with strong CO emission in the northern sky ($\delta \geqslant -35°$).[54] Additional galaxies with globally measured HCN emission data available in the literature are also included in the sample. Objects at Galactic latitudes $|b| < 10°$ are excluded due to the strong diffuse emission from the Galactic plane. Our final candidate list of 64 galaxies beyond the Local Group includes more than a dozen large nearby spiral galaxies, 22 LIRGs, and 9 ULIRGs. Global properties of the galaxies including RC luminosity, total IR luminosity, and HCN luminosity are provided in Table 1.

Many of the IR-bright starburst galaxies in our candidate list have been previously suggested as interesting targets for gamma-ray telescopes on the basis that a significant fraction of CR protons may interact in dense molecular clouds before escaping the ISM (Völk 1989; Akyüz et al. 1991; Paglione et al. 1996; Torres et al. 2004; Thompson et al. 2007). Furthermore, galaxies well known to host non-thermal leptonic populations are naturally included in this sample since diffuse radio emission associated with synchrotron radiation correlates with IR luminosity (Condon et al. 1991; Yun et al. 2001).

Some of the galaxies in our sample host radio-quiet AGNs with low-level jet activity. The galaxies associated with sources in the *Swift* BAT 58 month survey catalog (15–195 keV) with AGN-type designations (Baumgartner et al. 2010) are listed in the rightmost column of Table 1. Hard X-ray emission is a strong and relatively unbiased identifier of AGN activity (Burlon et al. 2011), while soft X-ray emission from AGNs is more often obscured by intervening circumnuclear and ISM material. X-ray emission from AGNs does not require the presence of a relativistic jet.

Five Local Group galaxies previously examined in LAT data are included in the multiwavelength comparisons appearing in Section 4.3. Multiwavelength data for those galaxies are summarized in Table 2.

The largest redshift of any galaxy in our sample is $z \sim 0.06$.

3. LAT OBSERVATIONS AND DATA ANALYSIS

The *Fermi*-LAT is a pair-production telescope with large effective area ($\sim$8000 cm^2 on axis for $E > 1$ GeV) and field of view ($\sim$2.4 sr at 1 GeV), sensitive to gamma rays in the energy range from 20 MeV to >300 GeV. Full details of the instrument and descriptions of the onboard and ground data processing are provided in Atwood et al. (2009), and information regarding on-orbit calibration procedures is given by Abdo et al. (2009a). The LAT normally operates in a scanning "sky-survey" mode which provides coverage of the full sky every two orbits ($\sim$3 hr). For operational reasons, the standard rocking angle (defined as the angle between the zenith and center of the LAT field of view) for survey mode was increased from 35° to 50° on 2009 September 3.

This work uses data collected in sky-survey mode from 2008 August 4 to 2011 August 4 for the analysis of 64 celestial

---

[54] The HCN survey includes galaxies with 60 μm/100 μm emission larger than 50 Jy/100 Jy and CO-line brightness temperatures larger than 100 mK for spirals or 20 mK for LIRGs/ULIRGs.

Table 1
Summary of the Star-forming Galaxy Sample: Beyond the Local Group

Galaxy	D (Mpc)	$L_{1.4\,\mathrm{GHz}}$ (10^{21} W Hz^{-1})	$L_{12\,\mu m}$ (10^{23} W Hz^{-1})	$L_{25\,\mu m}$	$L_{60\,\mu m}$	$L_{100\,\mu m}$	$L_{8-1000\,\mu m}$ (10^{10} $L_\odot$)	L_{HCN} (10^8 K km s^{-1} pc^2)	*Swift*-BAT Detected (AGN Classification)
NGC 253	2.5	4.18	0.307	1.16	7.24	9.63	2.1	0.27	...
M82	3.4	10.6	1.10	4.60	20.5	19.0	4.6	0.30	...
IC 342	3.7	3.69	0.244	0.565	2.96	6.42	1.4	0.47	...
NGC 4945	3.7	10.8	0.454	0.694	10.2	21.8	2.6	0.27	Sy2
M83	3.7	4.26	0.352	0.714	4.35	8.58	1.4	0.35	...
NGC 4826	4.7	0.268	0.0624	0.0756	0.970	2.16	0.26	0.040	...
NGC 6946	5.5	5.05	0.438	0.749	4.70	10.5	1.6	0.49	...
NGC 2903	6.2	2.06	0.243	0.397	2.78	6.00	0.83	0.090	...
NGC 5055	7.3	2.49	0.341	0.406	2.55	8.92	1.1	0.10	...
NGC 3628	7.6	3.63	0.216	0.335	3.79	7.31	1.0	0.24	...
NGC 3627	7.6	3.17	0.333	0.591	4.58	9.44	1.3	0.080	...
NGC 4631	8.1	9.42	0.405	0.704	6.70	12.6	2.0	0.080	...
NGC 4414	9.3	2.51	0.288	0.374	3.06	7.32	0.81	0.16	...
M51	9.6	16.4	0.795	1.05	10.7	24.4	4.2	0.50	...
NGC 891	10.3	8.90	0.669	0.889	8.44	21.9	2.6	0.25	...
NGC 3556	10.6	4.11	0.308	0.563	4.38	10.3	1.4	0.090	...
NGC 3893	13.9	3.30	0.335	0.381	3.60	8.51	1.2	0.23	...
NGC 660	14.0	9.08	0.715	1.71	15.4	26.9	3.7	0.26	...
NGC 5005	14.0	4.29	0.387	0.530	5.20	14.9	1.4	0.41	...
NGC 1055	14.8	5.58	0.587	0.744	6.12	17.1	2.1	0.37	...
NGC 7331	15.0	5.86	1.06	1.59	12.1	29.7	3.5	0.44	...
NGC 2146	15.2	29.7	1.89	5.20	40.6	53.6	10	0.96	...
NGC 3079	16.2	26.7	0.798	1.13	15.9	32.9	4.3	1.0	Sy2
NGC 1068	16.7	167	13.3	29.2	65.5	85.9	28	3.6	Sy2
NGC 4030	17.1	5.50	0.472	0.805	6.47	17.8	2.1	0.54	...
NGC 4041	18.0	4.04	0.438	0.605	5.49	12.3	1.7	0.18	...
NGC 1365	20.8	27.4	2.65	7.39	48.8	85.8	13	3.1	Sy1.8
NGC 1022	21.1	2.61	0.378	1.75	10.5	14.6	2.6	0.20	...
NGC 5775	21.3	15.2	0.993	1.34	12.8	30.2	3.8	0.57	...
NGC 5713	24.0	11.0	1.01	1.96	15.2	25.7	4.2	0.22	...
NGC 5678	27.8	10.3	0.869	1.11	8.94	23.7	3.0	0.75	...
NGC 520	31.1	20.5	1.04	3.73	36.5	54.8	8.5	0.64	...
NGC 7479	35.2	15.1	2.03	5.72	22.1	39.6	7.4	1.1	Sy2/LINER
NGC 1530	35.4	10.4	1.08	1.84	14.8	38.7	4.7	0.49	...
NGC 2276	35.5	40.7	1.61	2.46	21.5	43.7	6.2	0.40	...
NGC 3147	39.5	17.3	3.64	1.92	15.3	55.3	6.2	0.90	...
Arp 299	43.0	150	8.78	54.2	250	246	63	2.1	...
IC 5179	46.2	43.4	3.01	6.13	49.5	95.2	14	3.4	...
NGC 5135	51.7	64.2	2.01	7.61	53.9	99.0	14	2.7	...
NGC 6701	56.8	35.6	2.12	5.10	38.8	77.4	11	1.4	...
NGC 7771	60.4	62.3	4.32	9.47	85.9	175	21	6.5	...
NGC 1614	63.2	66.1	6.60	35.8	154	164	39	1.3	...
NGC 7130	65.0	96.4	2.93	10.9	84.5	131	21	3.3	Sy2/LINER
NGC 7469	67.5	98.7	8.67	32.5	149	192	41	2.2	Sy1.2
IRAS 18293−3413	72.1	141	7.09	24.8	222	332	54	4.0	...
Arp 220	74.7	218	4.07	53.4	695	770	140	9.2	...
Mrk 331	75.3	48.4	3.53	17.2	122	154	27	3.4	...
NGC 828	75.4	71.3	4.90	7.28	78.0	172	22	1.3	...
IC 1623	81.7	199	8.23	29.2	183	252	47	8.5	...
Arp 193	92.7	108	2.57	14.6	175	251	37	9.5	...
NGC 6240	98.1	492	6.79	40.9	264	305	61	11	Sy2
NGC 1144	117.3	256	4.58	10.4	87.3	187	25	2.7	Sy2
Mrk 1027	123.5	101	4.74	11.3	96.4	156	26	1.9	...
NGC 695	133.5	161	10.7	17.7	162	289	47	4.3	...
Arp 148	143.3	90.9	4.91	17.4	157	253	36	4.0	...
Mrk 273	152.2	403	6.65	65.4	624	624	130	15	...
UGC 05101	160.2	525	7.68	31.3	359	611	89	10	...
Arp 55	162.7	118	4.43	19.3	192	327	46	3.8	...
Mrk 231	170.3	1080	63.5	307	1070	1030	300	19	...
IRAS 05189−2524	170.3	102	25.7	120	460	411	120	6.2	...
IRAS 17208−0014	173.1	296	7.17	57.7	1150	1290	230	38	...
IRAS 10566+2448	173.3	208	7.19	45.6	435	539	94	10	...
VII Zw 31	223.4	245	11.9	37.0	329	603	87	9.8	...
IRAS 23365+3604	266.1	244	7.63	79.6	630	763	140	15	...

Notes. Galaxy distances, total IR (8–1000 μm) luminosities, and HCN-line luminosities are provided by Gao & Solomon (2004b). RC luminosities at 1.4 GHz come primarily from Yun et al. (2001), except for M82 and NGC 3627 (Condon et al. 1990), NGC 4945 (Wright & Otrupcek 1990), and Arp 299, NGC 5775, NGC 7331, and VII Zw 31 (Condon et al. 1998). Galaxies appearing in the *Swift* BAT 58 month survey catalog with AGN-type classification are identified (Baumgartner et al. 2010).

Table 2
Summary of Star-forming Galaxy Sample: Local Group Galaxies

Galaxy	D (Mpc)	$L_{1.4\,\mathrm{GHz}}$ $(10^{20}\,\mathrm{W\,Hz^{-1}})$	$L_{12\,\mu m}$	$L_{25\,\mu m}$ $(10^{22}\,\mathrm{W\,Hz^{-1}})$	$L_{60\,\mu m}$	$L_{100\,\mu m}$	$L_{8-1000\,\mu m}$ $(10^{9}\,L_{\odot})$	L_{HCN} $(10^{7}\,\mathrm{K\,km\,s^{-1}\,pc^{2}})$	$L_{0.1-100\,\mathrm{GeV}}$ $(10^{38}\,\mathrm{erg\,s^{-1}})$
SMC	0.06	0.19 ± 0.03	0.0029	0.012	0.29	0.65	0.07 ± 0.01	...	0.11 ± 0.03
LMC	0.05	1.3 ± 0.1	0.083	0.23	2.5	2.5	0.7 ± 0.1	...	0.47 ± 0.05
M33	0.85	2.8 ± 0.1	0.28	0.34	3.5	11	1.2 ± 0.2	...	<3.5
M31	0.78	6.3 ± 0.3	1.2	0.80	4.0	22	2.4 ± 0.4	...	4.6 ± 1.0
Milky Way	...	19 ± 6	12	7.2	16	46	14 ± 7	4 ± 2	8.2 ± 2.4

Notes. Global RC, IR, and gamma-ray luminosities of the Milky Way have been estimated using a numerical model of CR propagation and interactions in the ISM (Strong et al. 2010). Within the Local Group, an estimate for the global HCN-line luminosity is only available for the Milky Way (Solomon et al. 1992). Radio data for other Local Group galaxies: SMC (Loiseau et al. 1987), LMC (Hughes et al. 2007), M31 and M33 (Dennison et al. 1975). IR data for other Local Group galaxies come from Sanders et al. (2003). Gamma-ray data for other Local Group galaxies: SMC (Abdo et al. 2010h), LMC (Abdo et al. 2010e), M31 and M33 (Abdo et al. 2010b).

$15° \times 15°$ regions of interest (RoI) centered on the positions of the galaxies in our sample. We accept only low-background "source" class photon candidate events (Atwood et al. 2009) corresponding to the P7V6 instrument response functions with reconstructed energies 0.1–100 GeV. In order to reduce the effects of gamma rays produced by CR interactions in the upper atmosphere (Abdo et al. 2009b), we discard photons arriving from zenith angles $>100°$, exclude time periods when part of the RoI was beyond the zenith angle limit, and also exclude time periods when the spacecraft rocking angle exceeded $52°$.

The data were analyzed using the LAT Science Tools software package (version 09-25-02).[55] The model for each celestial RoI contains templates for the diffuse Galactic foreground emission (`gal_2yearp7v6_v0.fits`), a spectrum for the isotropic diffuse emission (composed of both photons and residual charged particle background, `iso_p7v6source.txt`), and all individual sources reported in the LAT 2 year source catalog (2FGL; Nolan et al. 2012) within $12°$ of the target galaxies. For the individual LAT sources, we assumed spectral models and parameters reported in the 2FGL catalog. The candidate sources corresponding to the galaxies in our sample were modeled as point sources with power-law spectra, $dN/dE \propto E^{-\Gamma}$, at the optically determined positions of the galaxies. Due to their typical angular sizes of $\mathcal{O}(0°.1)$ or smaller, and fluxes close to or below the LAT detection threshold, the galaxies considered in this work are not expected to be resolved as spatially extended beyond the energy-dependent LAT point-spread function (Lande et al. 2012).

The normalization and photon index of each gamma-ray source candidate were fitted using a maximum likelihood procedure suitable for the analysis of binned photon data (`gtlike`). The photons within each RoI were binned spatially into $0°.1$-sized pixels and into 30 energy bins uniformly spaced in log-energy (10 bins for each power of 10 in energy). During the maximum likelihood fitting, the normalizations of the diffuse components were left free. We also fit the normalizations of all neighboring LAT sources within $4°$ of the target galaxy positions, or located within the $15° \times 15°$ RoI and detected with exceptionally high significance in the 2FGL catalog.[56]

4. RESULTS

Results from the analysis of 64 galaxies beyond the Local Group in LAT data are presented first, followed by a discussion of multiwavelength relationships using the full sample of 69 star-forming galaxies.

4.1. LAT Data Analysis Results

Table 3 summarizes results from the maximum likelihood analyses. Source detection significance is determined using the test-statistic (TS) value, $\mathrm{TS} \equiv -2(\ln(L_0) - \ln(L_1))$, which compares the likelihoods of models including the galaxy under consideration (L_1) and the null hypothesis of no gamma-ray emission from the galaxy (L_0; Mattox et al. 1996). Significant ($\mathrm{TS} > 25$) gamma-ray excesses above background were detected in directions coinciding with four galaxies in the sample: two prototypical starburst galaxies, M82 and NGC 253, and two starburst galaxies also containing Seyfert 2 nuclei, NGC 1068, and NGC 4945. Each of the four gamma-ray sources is associated with the corresponding galaxy from our sample according to the 2FGL catalog (Nolan et al. 2012).

We additionally obtain relatively large TS values in the directions of NGC 2146 ($\sim$20) and M83 ($\sim$15). These excesses do not pass the conventional threshold of $\mathrm{TS} > 25$ required to claim a source detection. Lenain & Walter (2011) noted an excess in the vicinity of M83, but determined that the best-fit position was inconsistent with the galaxy location and instead proposed an association with the blazar 2E 3100. We will return to these two galaxies in Section 6.

CR-induced gamma-ray emission from galaxies is expected to be steady on the timescales of our observations. Variability is tested for the four significantly detected sources by partitioning the full observation period into 12 time intervals of $\sim$90 days each and performing a separate maximum likelihood fit for each of the shorter time periods. The resulting light curves are shown in Figure 1. None of the four sources show significant changes in flux over the 3 years of LAT observations. This finding is consistent with the results obtained by Lenain et al. (2010) for NGC 1068 and NGC 4945.

Spectral energy distributions of M82, NGC 253, NGC 1068, and NGC 4945 are shown in Figure 2. Each flux measurement represents a separate maximum likelihood fit following the procedures described above, but for six logarithmically spaced energy bins. Each energy bin is further divided into five logarithmically spaced sub-bins of energy for binned likelihood analysis to maintain $\sim$10 bins for each power of 10 in energy. Using the power-law spectral models, the maximum likelihood

---

[55] Information regarding the LAT Science Tools package, diffuse models, instrument response functions, and public data access is available from the Fermi Science Support Center (http://fermi.gsfc.nasa.gov/ssc/).
[56] More than 1000 attributed photons in the 2FGL data set or TS > 500; see Section 4.1 for the definition of TS value.

Table 3
Maximum Likelihood Analysis Results

Galaxy	D (Mpc)	$F_{0.1-100\,\mathrm{GeV}}$ (10^{-9} ph cm^{-2} s^{-1})	Γ	$L_{0.1-100\,\mathrm{GeV}}$ (10^{40} erg s^{-1})	TS
NGC 253	2.5	12.6 ± 2.0	2.2 ± 0.1	0.6 ± 0.2	109.4
M82	3.4	15.4 ± 1.9	2.2 ± 0.1	1.5 ± 0.3	180.1
IC 342	3.7	<2.7	2.2	0.3	...
NGC 4945	3.7	8.5 ± 2.8	2.1 ± 0.2	1.2 ± 0.4	33.2
M83	3.7	<7.0	2.2	0.8	...
NGC 4826	4.7	<2.9	2.2	0.6	...
NGC 6946	5.5	<1.6	2.2	0.4	...
NGC 2903	6.2	<2.5	2.2	0.8	...
NGC 5055	7.3	<2.1	2.2	1.0	...
NGC 3628	7.6	<3.1	2.2	1.6	...
NGC 3627	7.6	<3.5	2.2	1.7	...
NGC 4631	8.1	<1.6	2.2	0.9	...
NGC 4414	9.3	<3.1	2.2	2.3	...
M51	9.6	<3.2	2.2	2.6	...
NGC 891	10.3	<4.2	2.2	3.8	...
NGC 3556	10.6	<2.3	2.2	2.2	...
NGC 3893	13.9	<2.9	2.2	4.8	...
NGC 660	14.0	<3.0	2.2	5.0	...
NGC 5005	14.0	<3.4	2.2	5.7	...
NGC 1055	14.8	<2.9	2.2	5.5	...
NGC 7331	15.0	<1.7	2.2	3.2	...
NGC 2146	15.2	<6.7	2.2	13.2	...
NGC 3079	16.2	<2.2	2.2	5.0	...
NGC 1068	16.7	6.4 ± 2.0	2.2 ± 0.2	15.4 ± 6.1	38.1
NGC 4030	17.1	<3.0	2.2	7.6	...
NGC 4041	18.0	<3.7	2.2	10.3	...
NGC 1365	20.8	<2.5	2.2	9.4	...
NGC 1022	21.1	<2.2	2.2	8.5	...
NGC 5775	21.3	<1.6	2.2	6.4	...
NGC 5713	24.0	<1.8	2.2	9.0	...
NGC 5678	27.8	<2.8	2.2	18.3	...
NGC 520	31.1	<2.0	2.2	16.7	...
NGC 7479	35.2	<6.1	2.2	65.2	...
NGC 1530	35.4	<2.8	2.2	29.7	...
NGC 2276	35.5	<1.4	2.2	15.5	...
NGC 3147	39.5	<1.8	2.2	23.5	...
Arp 299	43.0	<3.1	2.2	49.3	...
IC 5179	46.2	<0.9	2.2	17.3	...
NGC 5135	51.7	<1.5	2.2	34.2	...
NGC 6701	56.8	<2.4	2.2	65.2	...
NGC 7771	60.4	<2.0	2.2	62.4	...
NGC 1614	63.2	<2.1	2.2	72.2	...
NGC 7130	65.0	<1.3	2.2	47.5	...
NGC 7469	67.5	<2.4	2.2	94.9	...
IRAS 18293−3413	72.1	<2.0	2.2	90.8	...
Arp 220	74.7	<4.4	2.2	209.6	...
Mrk 331	75.3	<1.5	2.2	71.9	...
NGC 828	75.4	<2.7	2.2	129.9	...
IC 1623	81.7	<1.8	2.2	100.6	...
Arp 193	92.7	<2.6	2.2	189.2	...
NGC 6240	98.1	<2.3	2.2	186.5	...
NGC 1144	117.3	<1.2	2.2	141.1	...
Mrk 1027	123.5	<5.6	2.2	731.8	...
NGC 695	133.5	<4.2	2.2	646.1	...
Arp 148	143.3	<5.2	2.2	923.8	...
Mrk 273	152.2	<2.9	2.2	582.0	...
UGC 05101	160.2	<1.3	2.2	287.4	...
Arp 55	162.7	<1.7	2.2	380.1	...
Mrk 231	170.3	<1.9	2.2	468.4	...
IRAS 05189−2524	170.3	<1.6	2.2	395.6	...
IRAS 17208−0014	173.1	<5.6	2.2	1434.0	...
IRAS 10566+2448	173.3	<2.0	2.2	521.0	...
VII Zw 31	223.4	<1.6	2.2	692.6	...
IRAS 23365+3604	266.1	<1.7	2.2	1059.0	...

Notes. Each galaxy is analyzed using a power-law spectral model, $dN/dE \propto E^{-\Gamma}$. Flux upper limits for galaxies not significantly detected in LAT data are presented at the 95% confidence level, assuming a photon index $\Gamma = 2.2$.
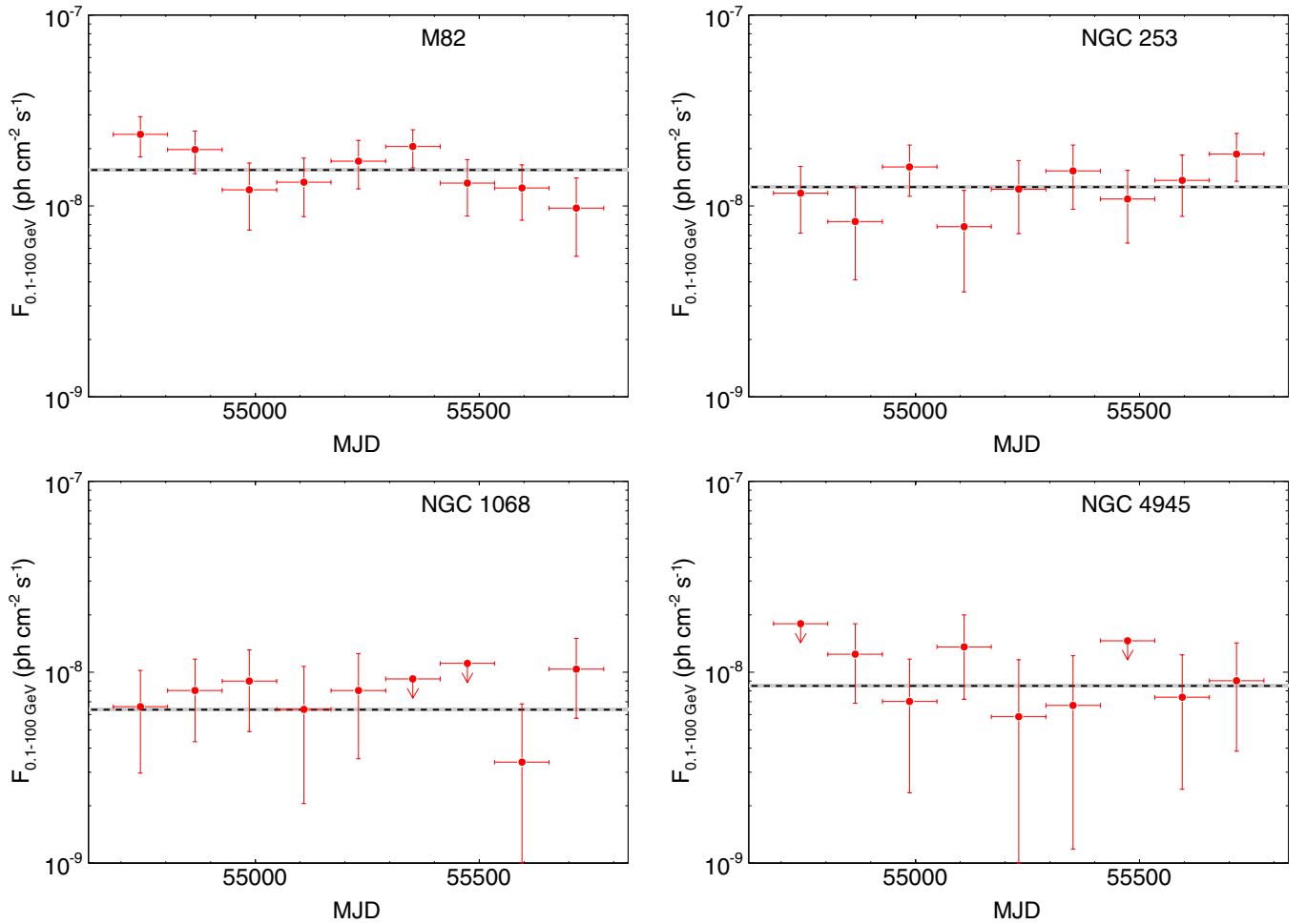
Figure 1. Gamma-ray light curves for four significantly detected galaxies. The full 3 year observation period was divided into 12 time intervals of ∼90 days each. A maximum likelihood fit was performed for each of the shorter time intervals to test for variability. The dashed black line shows the maximum likelihood flux level obtained for the full 3 year observation period. The gray band represents a 2% systematic uncertainty in source exposure resulting from small inaccuracies in the dependence of the instrument response on the source viewing angle, coupled with changes in the observing profile as the orbit of the spacecraft processes. Flux upper limits are shown at the 95% confidence level.

(A color version of this figure is available in the online journal.)

photon index values for the four galaxies are in the range 2.1–2.4. For M82 and NGC 253, the extrapolated power-law fits from the LAT energy range naturally connect with spectral measurements obtained by imaging air-Cerenkov telescopes at higher energies (Acciari et al. 2009; Acero et al. 2009; Ohm et al. 2011).

Integral flux upper limits in the range 0.1–100 GeV at the 95% confidence level are provided in Table 3 for galaxies not significantly detected by the LAT. Limits are computed using the profile likelihood technique, for which the flux of a target source is varied over a range while simultaneously maximizing the model likelihood with respect to all other parameters. One-sided 95% CL upper limits correspond to a decrease in profile likelihood, L_p, of $2\Delta \ln(L_p) = 2.71$ relative to the maximum likelihood. The flux upper limits presented in Table 3 are derived using a power-law spectral model with photon index $\Gamma = 2.2$, corresponding to the typical index of the four LAT-detected starbursts. The upper limits increase by 10%–20% (less constraining) on average when assuming a photon index of 2.3.

4.2. Gamma Rays from Starbursting Seyfert 2 Galaxies

NGC 1068 and NGC 4945 deserve special attention as galaxies with both circumnuclear starbursts and radio-quiet

obscured AGNs. The gamma-ray spectra of NGC 1068 and NGC 4945 are similar to those of M82 and NGC 253, and none of the four galaxies show indications of gamma-ray variability. Lenain et al. (2010) suggested a model for NGC 1068 in which gamma rays are produced mainly through inverse Compton scattering of IR photons by electrons in the misaligned jet at distances ∼0.1 pc from the central engine. In this scenario, NGC 1068 is viewed as the first member of a new class of gamma-ray sources.

Studies of X-ray-selected Seyfert galaxies using LAT data demonstrate that Seyfert galaxies hosting radio-quiet AGNs are generally gamma-ray quiet as a population (Teng et al. 2011; Ackermann et al. 2012b). Excepting NGC 1068 and NGC 4945, no other radio-quiet Seyfert galaxies have been detected by the LAT. The upper limits in 0.1–100 GeV luminosity inferred for several other nearby Seyfert galaxies are below the gamma-ray luminosity of NGC 1068 (Ackermann et al. 2012b). The tightest constraint is found for NGC 4151, located at a distance of 11.2 Mpc, with gamma-ray luminosity $<2 \times 10^{40}$ erg s^{-1} (a factor ∼10 below that of NGC 1068).

The relative contributions of CR interactions versus AGN activity to the gamma-ray emission of NGC 1068 and NGC 4945 are not yet definitively established. In the multiwavelength
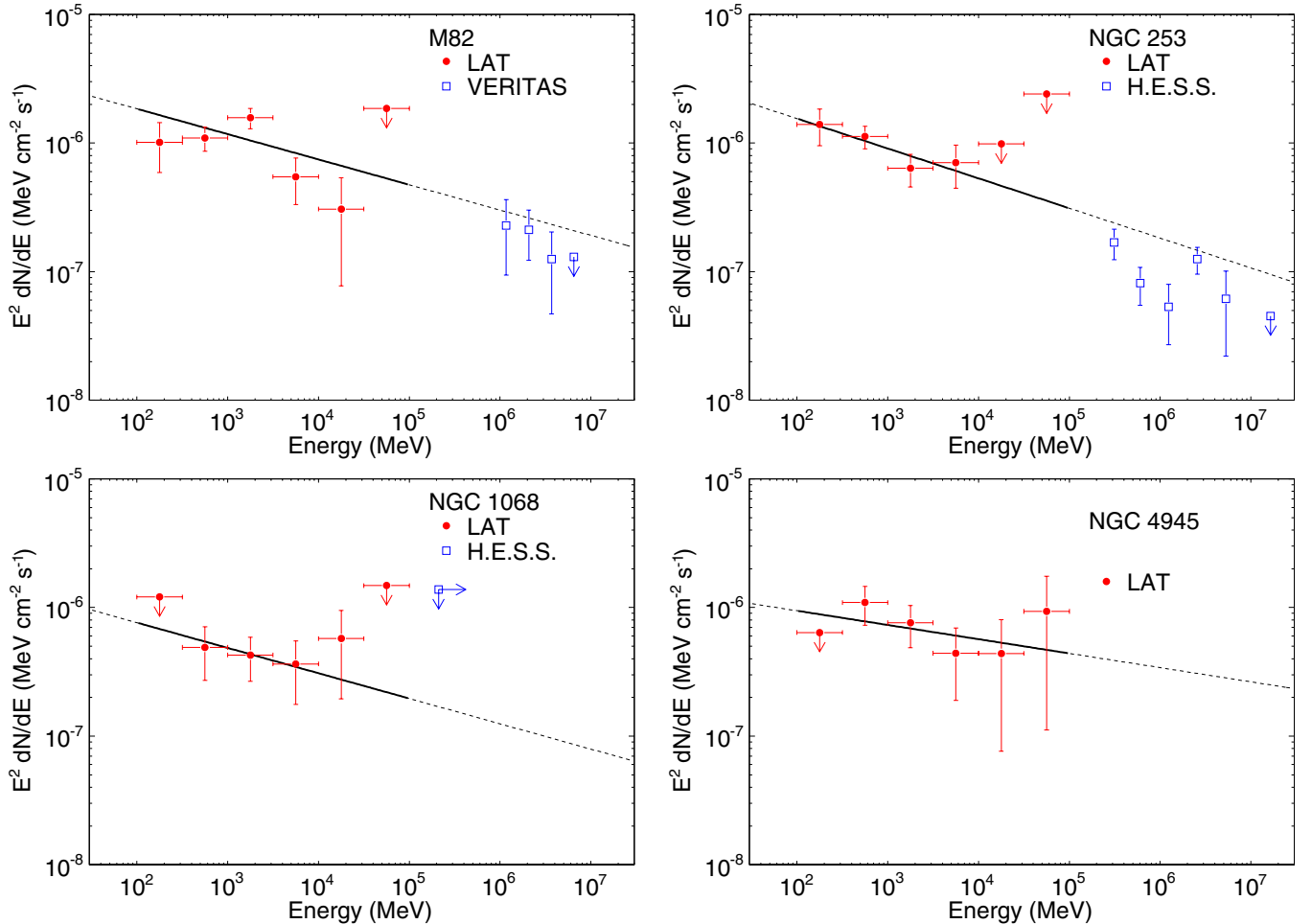
Figure 2. Spectral energy distributions for four starburst galaxies significantly detected in high-energy gamma rays. 95% confidence upper limits are indicated in energy bins with detection significance TS < 1. The best-fit power-law spectral model is shown for each galaxy in the energy range used for the maximum likelihood analysis (0.1–100 GeV, solid) and in extrapolation to neighboring wavebands (dashed). Flux measurements produced by imaging air-Cerenkov telescopes are included for M82 (VERITAS; Acciari et al. 2009) and NGC 253 (H.E.S.S.; Ohm et al. 2011), and flux upper limits above 210 GeV are shown for NGC 1068 (H.E.S.S.; Aharonian et al. 2005). The uncertainties depicted for LAT flux measurements represent combined statistical and systematic uncertainties.
(A color version of this figure is available in the online journal.)

analysis which follows, we will consider both the full sample of analyzed galaxies, and a subsample with galaxies hosting *Swift*-BAT-detected AGNs removed.

4.3. Multiwavelength Luminosity Comparisons

Many authors have proposed scaling relationships between galaxy SFRs and gamma-ray luminosities motivated by the connections between interstellar gas, star formation, SNe, and CRs (e.g., Pavlidou & Fields 2002; Torres et al. 2004; Thompson et al. 2007; Stecker 2007; Persic & Rephaeli 2010; Lacki et al. 2011). We now examine relationships between gamma-ray luminosity and several photometric tracers of star formation taking advantage of the 3 year accumulation of LAT data.

The radiative output of star-forming galaxies across much of the electromagnetic spectrum is related to the abundance of short-lived massive stars. Many photometric estimators of the recent star formation histories of galaxies have been used. Total IR luminosity 8–1000 μm is one well-established tracer of the SFR for late-type galaxies (reviewed by Kennicutt 1998a). The conversion proposed by Kennicutt (1998b),

$$\frac{\text{SFR}}{M_\odot \, \text{yr}^{-1}} = \epsilon \, 1.7 \times 10^{-10} \frac{L_{8-1000 \, \mu m}}{L_\odot}, \quad (1)$$

assumes that thermal emission of interstellar dust approximates a calorimetric measure of radiation produced by young (10–100 Myr) stellar populations. All SFRs quoted in this work consider the stellar mass range 0.1–100 $M_\odot$. The factor ϵ depends on the assumed initial mass function (IMF), with $\epsilon = 1$ for the Salpeter (1955) IMF originally used by Kennicutt (1998b). We will use $\epsilon = 0.79$ to convert[57] to the Chabrier (2003) IMF, proposed after further studies of star formation in the 0.1–1 $M_\odot$ mass range.

Several other photometric SFR estimators have been calibrated using the Kennicutt (1998b) total IR luminosity relation. These include RC luminosity at 1.4 GHz produced by synchrotron-emitting CR electrons (Yun et al. 2001),
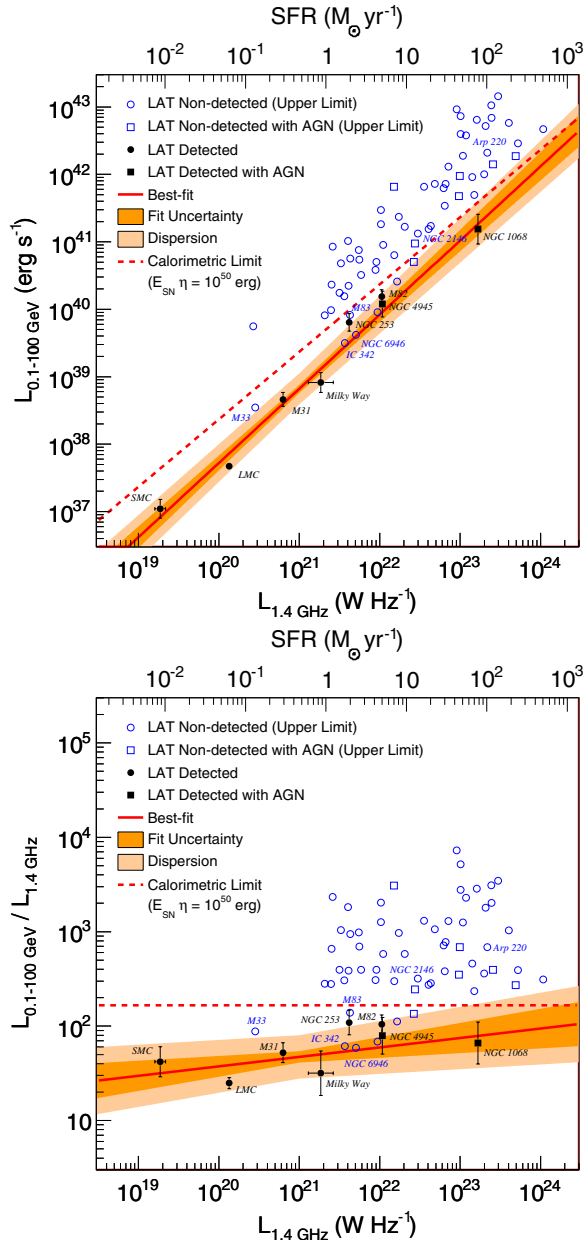
$$\text{SFR}(M_\odot \, \text{yr}^{-1}) = \epsilon (5.9 \pm 1.8) \times 10^{-22} L_{1.4 \, \text{GHz}}(\text{W Hz}^{-1}), \quad (2)$$

and HCN $J = 1$–0 line luminosity indicating the quantity of dense molecular gas available to form new stars (Gao & Solomon 2004b),

$$\text{SFR}(M_\odot \, \text{yr}^{-1}) = \epsilon \, 1.8 \times 10^{-7} L_{\text{HCN}}(\text{K km s}^{-1} \, \text{pc}^2). \quad (3)$$

---

[57] We use the conversion factor proposed by Crain et al. (2010) for SFRs estimated from total IR luminosity: $\text{SFR}_{\text{Chabrier}} = 0.79 \, \text{SFR}_{\text{Salpeter}}$.
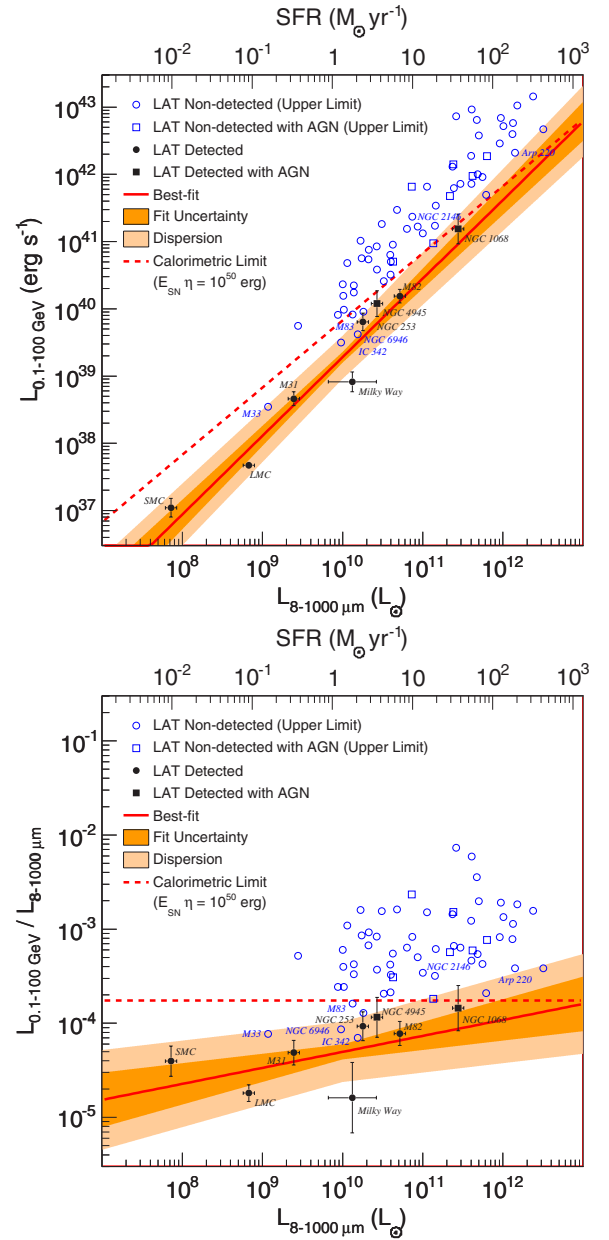
Figure 3. Top panel: gamma-ray luminosity (0.1–100 GeV) vs. RC luminosity at 1.4 GHz. Galaxies significantly detected by the LAT are indicated with filled symbols whereas galaxies with gamma-ray flux upper limits (95% confidence level) are marked with open symbols. Galaxies hosting *Swift*-BAT AGNs are shown with square markers. RC luminosity uncertainties for the non-detected galaxies are omitted for clarity, but are typically less than 5% at a fixed distance. The upper abscissa indicates SFR estimated from the RC luminosity according to Equation (2) (Yun et al. 2001). The best-fit power-law relation obtained using the EM algorithm is shown by the red solid line along with the fit uncertainty (darker shaded region), and intrinsic dispersion around the fitted relation (lighter shaded region). The dashed red line represents the expected gamma-ray luminosity in the calorimetric limit assuming an average CR luminosity per supernova of $E_{SN} \eta = 10^{50}$ erg (see Section 5.1). Bottom panel: ratio of gamma-ray luminosity (0.1–100 GeV) to RC luminosity at 1.4 GHz.

(A color version of this figure is available in the online journal.)

Although these three SFR estimators are intrinsically linked, each explores a different stage of stellar evolution and is subject to different astrophysical and observational systematic uncertainties.

Figures 3 and 4 compare the gamma-ray luminosities of galaxies in our sample to their differential luminosities at 1.4 GHz, and total IR luminosities (8–1000 μm), respectively.

Figure 4. Same as Figure 3, but showing gamma-ray luminosity (0.1–100 GeV) vs. total IR luminosity (8–1000 μm). IR luminosity uncertainties for the non-detected galaxies are omitted for clarity, but are typically ∼0.06 dex. The upper abscissa indicates SFR estimated from the IR luminosity according to Equation (1) (Kennicutt 1998b).

(A color version of this figure is available in the online journal.)

A second abscissa axis has been drawn on each figure to indicate the estimated SFR corresponding to either RC or total IR luminosity using Equations (2) and (1). The upper panels of Figures 3 and 4 directly compare luminosities between wavebands, whereas the lower panels compare luminosity ratios. Taken at face value, the two figures show a clear positive correlation between gamma-ray luminosity and SFR, as has been reported previously in LAT data (see in this context Abdo et al. 2010b). However, sample selection effects, and galaxies not yet detected in gamma rays must be taken into account to properly determine the significance of the apparent correlations.

We test the significances of multiwavelength correlations using the modified Kendall τ rank correlation test proposed by Akritas & Siebert (1996). This method is an example of "survival
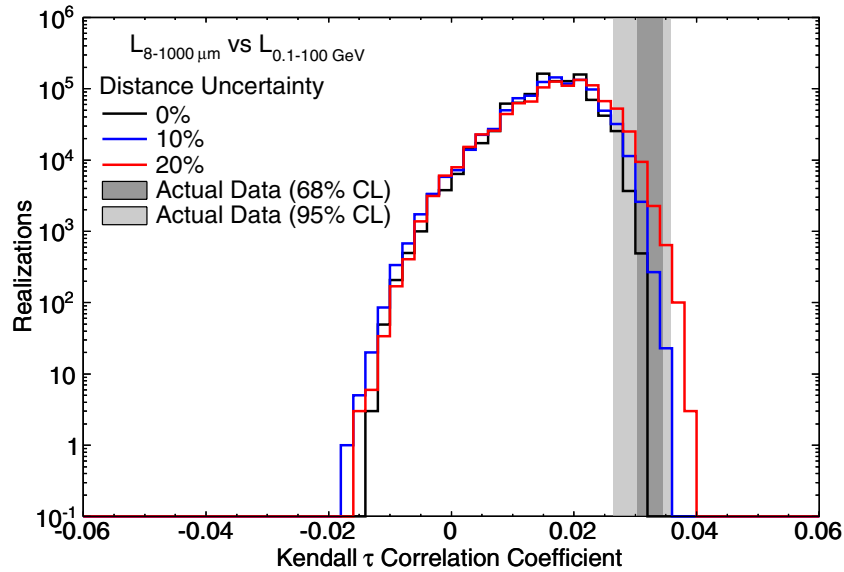
Figure 5. Graphical representation of the method adopted to estimate significances of multiwavelength correlations using the Kendall τ statistic. Total IR luminosity (8–1000 μm) and gamma-ray luminosity (0.1–100 GeV) are compared using the full sample of 69 galaxies in this example. Null hypothesis distributions of correlation coefficients assuming independence between wavebands are shown for three levels of uncertainty in distance measurements (one standard deviation of the scatter). The null hypothesis distributions are generated from 10^6 permutations of gamma-ray luminosities among the galaxies, requiring that the resultant gamma-ray fluxes could have been measurable given the flux sensitivity threshold of the LAT. The correlation efficient of the actual data is represented as a probability density to account for uncertainty in measured gamma-ray fluxes. The gray bands indicate the inner 68% and 95% of the probability density for the actual data. The correlation significance is estimated by computing the fraction of null hypothesis realizations with correlation coefficient larger than that obtained for the actual data (i.e., the P-value). See Section 4.3 and Appendix A for details.

(A color version of this figure is available in the online journal.)

analysis" techniques, suitable for the analysis of partially censored data sets (i.e., containing a mixture of detections and upper limits). The Kendall τ coefficient, $\tau \in [-1, 1]$, indicates the degree of positive or negative correlation between two quantities by comparing the ordering of each pair of points in the data set. For example, $\tau = 1$ describes a set of uncensored data points which are monotonically increasing. This non-parametric approach makes no assumption regarding the particular mathematical form for the relationship between compared quantities. See Appendix A for a detailed description of the method.

The multiwavelength relationships are tested in luminosity space because we are primarily interested in the intrinsic galaxy properties, and importantly, because multiwavelength comparisons in flux space can either falsely suggest a non-existent correlation or obscure a genuine physical correlation if the underlying relationship between intrinsic luminosities is nonlinear (Feigelson & Berg 1983; Kembhavi et al. 1986; and see Appendix B). We performed a series of Monte Carlo simulations to investigate potential biases resulting from selection effects for flux-limited samples of objects compared in luminosity space. The generalized Kendall τ correlation test is found to be robust against the selection effects expected for our application. A brief discussion of results from that study is presented in Appendix C.

Significances of the multiwavelength relationships are computed by comparing the τ correlation coefficient of the actual data to the distribution of τ correlation coefficients which could be obtained under the null hypothesis of independence between wavebands. Null hypothesis data sets are generated by scrambling derived gamma-ray luminosities among galaxies. Only "observable" permutations are retained to account for the truncation of measurable gamma-ray luminosities imposed by the LAT flux sensitivity (following the method of Efron & Petrosian 1999). Specifically, we require that the resultant gamma-ray flux

(or upper limit) of each galaxy in a scrambled data set could have been measurable by the LAT in order for the scrambled data set to be included in the null hypothesis distribution. In practice, each permutation represents an exchange of gamma-ray luminosities between two randomly selected galaxies so that statistically meaningful null hypothesis distributions can be efficiently generated. Gamma-ray flux sensitivity thresholds are determined by randomly sampling from the distribution of gamma-ray flux upper limits presented in Table 3 for each galaxy in the pair to be exchanged. We perform 1000 such exchanges on the actual data before counting permutations toward the null hypothesis distribution.

Inaccuracies in the distance measurements to the galaxies are included in our analysis because these errors are propagated in the transformation of measured fluxes into luminosities. Scatter in distance measurements applied to a collection of objects tends to broaden the distribution of objects in luminosity space, and can therefore induce positive correlation. For the galaxies in our sample at distances $1 \, \text{Mpc} \lesssim D \lesssim 100 \, \text{Mpc}$, the typical distance measurement precision for individual galaxies is 10%–20% (Freedman et al. 2001, and references therein). For our particular sample, we can compare the distances provided in the HCN survey of Gao & Solomon (2004a) to those reported in the IRAS Revised Bright Galaxies Sample (Sanders et al. 2003), and find that for galaxies beyond the Local Group, the average discrepancy between reported distances is 10%. We assume that measurement errors are normally distributed and centered on the true distances to the galaxies.

Figure 5 shows an example of the correlation significance test applied to the relationship between gamma-ray and IR luminosity using the full sample of star-forming galaxies. The distribution of correlation coefficients for 10^6 "observable" permutations of the actual data is plotted for three levels of distance measurement scatter. The null hypothesis distributions

Table 4
Scaling Relationships between Global Luminosities: Non-parametric Analysis of Correlation Significance

	Full Sample			Excluding AGN		
	$\sigma_D = 0\%$	$\sigma_D = 10\%$	$\sigma_D = 20\%$	$\sigma_D = 0\%$	$\sigma_D = 10\%$	$\sigma_D = 20\%$
$L_{1.4\,\mathrm{GHz}}$: $L_{0.1-100\,\mathrm{GeV}}$	0.001	0.005	0.01	0.007	0.03	0.06
$L_{8-1000\,\mu\mathrm{m}}$: $L_{0.1-100\,\mathrm{GeV}}$	0.0003	0.001	0.005	0.0004	0.004	0.02
L_{HCN}: $L_{0.1-100\,\mathrm{GeV}}$	0.05	0.07	0.1	0.2	0.3	0.4

Notes. Results for the Kendall τ significance tests for correlation between gamma-ray luminosity and each of RC luminosity, IR luminosity, and HCN-line luminosity, expressed as P-values representing the probabilities of erroneously rejecting the null hypothesis that no correlation exists between wavebands. A description of the Kendall τ statistic is provided in Appendix A and details of the implementation are provided in Section 4.3. Scatter in the distance measurements to the galaxies are assumed to be normally distributed with standard deviation (σ_D) expressed as a percentage of the actual galaxy distances.

tend toward positive values due to the truncation of measurable gamma-ray luminosities, effectively requiring a larger correlation coefficient for the actual data in order to claim a significant relationship between wavebands. As the level of scatter in distance measurements is increased, the tails of null hypothesis distributions extend to larger positive values. The probability that a null hypothesis data set would have a correlation coefficient larger than that of the actual data corresponds to the P-value measure of correlation significance.

Given uncertainties for the measured gamma-ray fluxes of galaxies in our sample, the correlation coefficient of the actual data is more appropriately viewed as a probability density as opposed to a single value (the Kendall τ statistic does not explicitly include measurement errors). To account for this uncertainty, we draw a flux value for each LAT-detected galaxy from a normal distribution centered on the best-fit flux with standard deviation equal to the reported flux uncertainty. A correlation coefficient is then computed using the sampled gamma-ray fluxes. This process is repeated many times to generate a distribution of correlation coefficients representing the actual data, as shown by the gray bands in Figure 5. Finally, we integrate over the probability density of correlation coefficients representing the actual data to obtain significances for the multiwavelength relations.

The results of the correlation tests are summarized in Table 4. Using the full sample of 69 star-forming galaxies, the null hypothesis of independence between gamma-ray luminosity and either RC or total IR luminosity can be rejected at the $\gtrsim 99\%$ confidence level allowing for 20% uncertainty on the distance measurements to the galaxies. No evidence for a correlation between gamma-ray luminosity and HCN-line luminosity is found in this study, an apparent discrepancy considering the previously established correlations between RC, IR, and HCN-line luminosities (Liu & Gao 2010). However, global HCN-line luminosity estimates are not available for the SMC and LMC, M31, and M33, which effectively reduces the luminosity range over which the correlation between wavebands can be tested, and excludes three LAT-detected galaxies from the analysis.

We also considered the more conservative case in which galaxies hosting *Swift*-BAT-detected AGNs, including NGC 1068 and NGC 4945 along with seven others, were removed from the sample given the potential contributions of the AGN to the broadband emission of those galaxies. In that case, the P-values for the correlations between gamma-ray luminosity and either RC or IR luminosity are ~ 0.05 allowing for 20% uncertainty on the distance measurements.

Even in the most conservative case described above, the data prefer a correlation between gamma-ray luminosity and both RC and IR luminosity. Although strong conclusions regarding

the significance of the multiwavelength correlations cannot be made at the time, at minimum, scaling relations derived from the current sample have predictive value and offer a testable hypothesis for further observations.

We fit scaling relationships between wavebands using simple power-law forms. For example,

$$\log\left(\frac{L_{0.1-100\,\mathrm{GeV}}}{\mathrm{erg\,s^{-1}}}\right) = \alpha \log\left(\frac{L_{8-1000\,\mu\mathrm{m}}}{10^{10}L_\odot}\right) + \beta \qquad (4)$$

parameterizes the relationship between gamma-ray and total IR luminosity.

Two regression methods are employed: the expectation-maximization (EM) algorithm, and the Buckley–James algorithm. The EM algorithm is similar to the least-squares fitting method, and assumes that the intrinsic residuals of gamma-ray luminosity are normally distributed in log space about the regression line for fixed values of either RC or IR luminosity. Non-detections are incorporated in the regression analysis by determining the degree to which the upper limits are compatible with the assumed dispersion about the regression line. The variance of the intrinsic residuals becomes a third parameter in the fit. The Buckley–James algorithm is similar in approach, but generalizes to cases for which the intrinsic distribution of residuals relative to the regression line is not normally distributed. Instead, the intrinsic dispersion is estimated using the Kaplan–Meier distribution obtained from the scatter within the data set itself. Isobe et al. (1986) provide details regarding the theory and implementation several commonly used survival analysis methods including the EM and Buckley–James regression algorithms.

Table 5 reports the best-fits of gamma-ray luminosity versus either RC luminosity or total IR luminosity, which were evaluated using the ASURV Rev 1.2 code (LaValley et al. 1992).[58] The two regression methods yield consistent results. For both the RC and total IR tracers of SFR, a nearly linear power-law index of $\alpha = 1.0$–1.2 is preferred. The scaling indices between gamma-ray luminosity and SFR tracers found for the larger sample of galaxies is consistent within uncertainties with that obtained considering the Local Group galaxies alone, $\alpha = 1.4 \pm 0.3$ (Abdo et al. 2010b). In particular, the gamma-ray luminosity upper limits found for LIRGs and ULIRGs disfavor a strongly nonlinear scaling relation. Table 5 also contains regression parameters fitted after removing galaxies hosting *Swift*-BAT-detected AGNs from the sample, which would be appropriate if the broadband emissions of those galaxies were heavily

---

[58] ASURV and other tools for the analysis of censored data sets are available from the Penn State Center for Astrostatistics (http://www.astrostatistics.psu.edu/statcodes/sc_censor.html).

Table 5
Scaling Relationships between Global Luminosities: Power-law Fits with Full Sample

	Expectation-maximization Method			Buckley–James Method		
	α	β	$\sqrt{\text{Variance}}$	α	β	$\sqrt{\text{Variance}}$
Full sample of galaxies						
$L_{1.4\,\text{GHz}}$: $L_{0.1-100\,\text{GeV}}$ $(10^{21}\,\text{W Hz}^{-1})$: (erg s^{-1})	1.10 ± 0.05	38.82 ± 0.06	0.17	1.10 ± 0.06	38.81	0.20
$L_{8-1000\,\mu\text{m}}$: $L_{0.1-100\,\text{GeV}}$ $(10^{10}\,L_\odot)$: (erg s^{-1})	1.17 ± 0.07	39.28 ± 0.08	0.24	1.18 ± 0.10	39.31	0.31
Excluding galaxies hosting *Swift*-BAT-detected AGN						
$L_{1.4\,\text{GHz}}$: $L_{0.1-100\,\text{GeV}}$ $(10^{21}\,\text{W Hz}^{-1})$: (erg s^{-1})	1.10 ± 0.07	38.81 ± 0.07	0.19	1.09 ± 0.11	38.80	0.24
$L_{8-1000\,\mu\text{m}}$: $L_{0.1-100\,\text{GeV}}$ $(10^{10}\,L_\odot)$: (erg s^{-1})	1.09 ± 0.10	39.19 ± 0.10	0.25	1.10 ± 0.14	39.22	0.33

Notes. Fitted parameters for relationships between gamma-ray luminosity and multiwavelength tracers of star formation. Using the RC case as an example, the scaling relations are of the form $\log L_{0.1-100\,\text{GeV}} = \alpha \log L_{1.4\,\text{GHz}} + \beta$, with luminosities expressed in the units provided in the leftmost column. The square root of the variance provides an estimate of the intrinsic dispersion of gamma-ray luminosity residuals in log space about the best-fit regression line. For the EM algorithm, the intrinsic residuals about the best-fit line are assumed to be normally distributed in log space. The Buckley–James algorithm uses the Kaplan–Meier method to estimate the distribution of residuals. See Section 4.3 for a description of the fitting methods. Both the complete sample of 69 galaxies (containing eight LAT sources) and a subsample of 60 galaxies excluding the AGN detected by the *Swift* BAT are analyzed (containing six LAT sources).

influenced by AGN activity. The fitted parameters in both cases are consistent within statistical uncertainties.

Note that the intrinsic dispersion values presented in Table 5 should be viewed as upper limits because we have not made an attempt to account for measurement uncertainties in the gamma-ray fluxes.

The best-fit power laws obtained using the EM algorithm are plotted in Figures 3 and 4. The darker shaded regions represent uncertainty in the fitted parameters from the regression and the lighter shaded regions indicate the addition of intrinsic residuals to one standard deviation. None of the limits from non-detected galaxies are in strong conflict with the best-fit relations.

Luminosity ratios of the form shown in the lower panels of Figures 3 and 4 have a direct physical meaning in terms of the energy radiated in different parts of the electromagnetic spectrum. For a galaxy with non-thermal emission powered mainly by CR interactions, and having an SFR of $1\,M_\odot\,\text{yr}^{-1}$ (similar to the MW), the corresponding luminosity ratios between wavebands are

$$\log\left(\frac{L_{0.1-100\,\text{GeV}}}{L_{1.4\,\text{GHz}}}\right) = 1.7 \pm 0.1_{\text{(statistical)}} \pm 0.2_{\text{(dispersion)}}, \quad (5)$$

and

$$\log\left(\frac{L_{0.1-100\,\text{GeV}}}{L_{8-1000\,\mu\text{m}}}\right) = -4.3 \pm 0.1_{\text{(statistical)}} \pm 0.2_{\text{(dispersion)}}, \quad (6)$$

found using the full sample of galaxies with the EM regression algorithm.

Further gamma-ray observations are required to conclusively establish the multiwavelength correlations examined in this section. Additional data may also show that scaling relations beyond simple power-law forms are required once farther and more active sources are either detected or are constrained by more stringent gamma-ray upper limits.

5. DISCUSSION

In recent years, increasingly sensitive observations of external galaxies at both GeV and TeV energies have shown that starburst
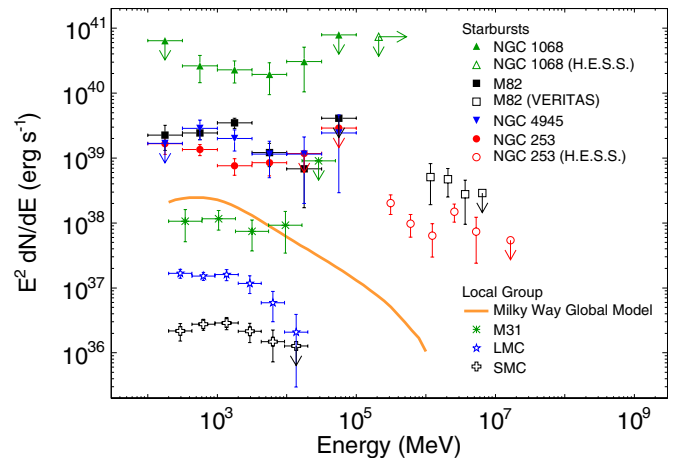
Figure 6. Gamma-ray luminosity spectra of star-forming galaxies detected by the LAT and imaging air-Cerenkov telescopes.
(A color version of this figure is available in the online journal.)

galaxies such as M82 and NGC 253 are characterized by harder gamma-ray spectra relative to quiescent galaxies of the Local Group (Acero et al. 2009; Acciari et al. 2009; Abdo et al. 2010d; Ohm et al. 2011), and that global gamma-ray luminosities of galaxies likely scale quasi-linearly with SFRs (e.g., Abdo et al. 2010b, 2010d; Lenain & Walter 2011).

Figure 6 compares the spectra of eight star-forming galaxies detected by gamma-ray telescopes. The more luminous galaxies also have comparatively harder gamma-ray spectra. Whereas the power-law spectral indices of M82 and NGC 253 are 2.2–2.3 extending to TeV energies, the spectra of the LMC and SMC steepen above ∼2 GeV (Abdo et al. 2010e, 2010h).

Scaling relations of the type examined in Section 4.3, and the observed gamma-ray spectra of star-forming galaxies, have implications both for the physics of CRs in the ISM and for the contribution of star-forming galaxies to the isotropic diffuse gamma-ray emission. In this section, we concentrate on the global non-thermal radiation features of star-forming galaxies from a population standpoint.

5.1. Physics of Cosmic Rays in Star-forming Galaxies

A discussion of scaling relations for diffuse gamma-ray radiation from star-forming galaxies invites comparison with the extensively studied RC–IR correlation. The RC–IR correlation extends over multiple galaxy types including irregulars, spirals, and ellipticals with ongoing star formation (de Jong et al. 1985; Wunderlich et al. 1987; Dressel 1988; Wrobel & Heeschen 1988, 1991), covers galaxies with magnetic energy densities likely ranging at least four orders of magnitude (Condon et al. 1991; Thompson et al. 2006), and applies to galaxies out to at least $z \sim 1$ (Appleton et al. 2004). High-resolution imaging has also shown the correlation to hold on $\sim$100 pc scales within individual galaxies (Marsh & Helou 1995; Paladino et al. 2006; Murphy et al. 2006).

A simple model proposed to explain the RC–IR correlation posits that galaxies are effective "calorimeters" of both UV photons and CR electrons (Völk 1989). In this picture, if the ISM is optically thick to UV photons, reprocessed starlight emitted in the IR becomes a proxy for the abundance of massive stars, and hence SFR. The luminosity of CR electrons is assumed to be proportional to the SFR in the basic calorimeter model. If either synchrotron losses dominate for CR electrons, or if the ratio of synchrotron losses to other loss mechanisms is uniform for many galaxy types, then the RC luminosity should also increase together with the SFR. The latter possibility requires some degree of fine-tuning (but see Lacki et al. 2010). Numerical models of CR propagation in the MW suggest that our Galaxy is an effective CR electron calorimeter (Strong et al. 2010).

Gamma-ray observations extend our study of CRs to include hadronic populations beyond the solar system, and notably, to measure the large-scale propagated spectra of CR nuclei in the MW and other galaxies. At energies above the threshold for pion production, hadronic gamma rays have the same spectral index as the underlying CR proton spectrum in the thin-target regime relevant for proton–proton interactions in the ISM. Diffuse pionic gamma rays presumably offer direct access to the majority of CR energy content, although leptonic diffuse emission and individual sources within galaxies must also contribute to the total emission. The gamma-ray spectra of the SMC and LMC are both consistent with models in which pionic gamma rays dominate the high-energy emission (Abdo et al. 2010e, 2010h). Many authors have argued that the majority of starburst emission at energies >0.1 GeV is produced by interactions of CR nuclei in the ISM, assuming primary CR proton to electron ratios similar to values found in the MW (e.g., Paglione et al. 1996; Torres 2004; Persic et al. 2008; Lacki et al. 2010).

For the MW in particular, global CR-induced gamma-ray emission above 0.1 GeV stems mostly from neutral pion decay (Bloemen 1985; Bertsch et al. 1993), with leptonic processes contributing 30%–40% in the energy range 0.1–100 GeV (Strong et al. 2010). The diffuse neutral pion decay component for the MW has spectral index $\sim$2.75 above $\sim$1 GeV, matching the locally measured CR proton spectrum (Simpson 1983; Sanuki et al. 2000; Adriani et al. 2011). CR escape from the MW plays a major role in the formation of the measured CR spectrum, but other galaxies with higher concentrations of ambient gas may work differently, behaving as calorimeters of CR nuclei, as suggested by Thompson et al. (2007). Approximately, 10% (possibly up to 20%) of the global gamma-ray emission of the MW is thought to originate from individual sources (Strong 2007).

We now review models for the interactions of CR nuclei to examine physical quantities involved in the scaling of hadronic gamma-ray emission, following the formalism of recent works by Persic & Rephaeli (2010) and Lacki et al. (2011). Neutral pion decay emission is related both to the energy density of CR nuclei, U_p, and to the ambient gas density, n, which serves as target material for inelastic collisions. The total hadronic gamma-ray luminosity (erg s^{-1}) can be expressed as

$$L_{\gamma,\pi^0} = \int_V \int E_\gamma \frac{dq}{dE_\gamma} \, n(\boldsymbol{r}) \, U_p(\boldsymbol{r}) dE_\gamma dV, \quad (7)$$

integrating over gamma-ray energies, E_γ, and over the whole galactic volume, V, which comprises the disk and surrounding halo occupied by CRs. The factor $q(\geqslant E_\gamma)$ denotes gamma-ray emissivity (s^{-1} H-atom^{-1} eV^{-1} cm^3) normalized to the CR energy density (Drury et al. 1994). Next, we define an average *effective* density of ambient gas encountered by CR nuclei:

$$\langle n_{\text{eff}} \rangle = \frac{\int_V n(\boldsymbol{r}) U_p(\boldsymbol{r}) dV}{\int_V U_p(\boldsymbol{r}) dV}. \quad (8)$$

Note that $\langle n_{\text{eff}} \rangle$ can be substantially lower than the average gas density found in the galaxy disk. CR nuclei of the MW are thought to spend most of their time in the low-gas-density halo, based upon combined measurements of unstable isotopes and spallation products (e.g., the B/C ratio) in the locally observed CR composition (reviewed by Strong et al. 2007). Using the above definition for the average effective gas density, Equation (7) separates to

$$L_{\gamma,\pi^0} = \int_V U_p dV \times \langle n_{\text{eff}} \rangle \times \int E_\gamma \frac{dq}{dE_\gamma} dE_\gamma. \quad (9)$$

The leading factor of Equation (9) represents the total energy of CR nuclei, and can be re-written as the product of the total luminosity of CR nuclei, L_p, and their characteristic residence time in the galactic volume, τ_{res}:

$$\int_V U_p dV = L_p \, \tau_{\text{res}}. \quad (10)$$

The trailing factor of Equation (9) depends upon the parent spectrum of CR nuclei, for which we assume a power-law spectral distribution, $dN_p/dP_p \propto (P_p \text{ GeV}^{-1} c)^{-\Gamma_p}$, where P_p is the momentum. Gamma-ray emissivities (s^{-1} H-atom^{-1} cm^3) in the energy range 0.1–100 GeV,

$$Q_{0.1-100\,\text{GeV}} = \int_{0.1\,\text{GeV}}^{100\,\text{GeV}} E_\gamma \frac{dq}{dE_\gamma} dE_\gamma, \quad (11)$$

are computed using the proton–proton interaction cross section parameterizations of Kamae et al. (2006). Note that the emissivities are normalized to the average energy density of CR nuclei (kinetic energies 1–10^6 GeV) within the entire galactic volume. A nuclear enhancement factor of 1.85 is included to account for heavy nuclei in both CRs and target matter (Mori 2009). The emissivities for $\Gamma_p = 2$–3 range from $Q_{0.1-100\,\text{GeV}} = (5.7$–$7.9) \times 10^{-17}$ s^{-1} H-atom^{-1} cm^3.

Substituting Equations (10) and (11) into Equation (9) yields

$$L_{0.1-100\,\text{GeV},\pi^0} = L_p \, \tau_{\text{res}} \, \langle n_{\text{eff}} \rangle \, Q_{0.1-100\,\text{GeV}}. \quad (12)$$

In the paradigm that SNRs are the primary sources of galactic CRs (Ginzburg & Syrovatskii 1964), CR luminosity is the

product of the SN rate, $\Gamma_{\rm SN}$, the kinetic energy released per SN, $E_{\rm SN}$, and the fraction of kinetic energy going into CR nuclei with kinetic energies >1 GeV (i.e., acceleration efficiency), η:

$$L_{\rm p} = \Gamma_{\rm SN}\, E_{\rm SN}\, \eta. \qquad (13)$$

Core-collapse SN rates can be estimated from SFRs given an IMF and a minimum stellar mass required to produce a core-collapse SN, which we take to be $8\,M_\odot$. For a Chabrier (2003) IMF, the transformation between SFR in the mass range 0.1–$100\,M_\odot$ and core-collapse SN rate is $\Gamma_{\rm SN}\Psi = {\rm SFR}$, with $\Psi = 83\,M_\odot$. The average kinetic energy released per core-collapse SN is $E_{\rm SN} \sim 10^{51}$ erg (Woosley & Weaver 1995). The gamma-ray luminosity becomes

$$L_{0.1-100\,{\rm GeV},\pi^0} = \Psi^{-1}\, {\rm SFR}\, E_{\rm SN}\, \eta\, \tau_{\rm res}\, \langle n_{\rm eff}\rangle\, \mathcal{Q}_{0.1-100\,{\rm GeV}}. \qquad (14)$$

Greater physical intuition can be realized by inserting values for the physical quantities similar to those of the MW,

$$L_{0.1-100\,{\rm GeV},\pi^0} = 9.4 \times 10^{38}\,{\rm erg\,s^{-1}} \left(\frac{\rm SFR}{M_\odot\,{\rm yr^{-1}}}\right)\left(\frac{E_{\rm SN}}{10^{51}\,{\rm erg}}\right)$$
$$\times \left(\frac{\eta}{0.1}\right)\left(\frac{\tau_{\rm res}}{10^7\,{\rm yr}}\right)\left(\frac{\langle n_{\rm eff}\rangle}{{\rm cm^{-3}}}\right), \qquad (15)$$

assuming a power-law index for CR nuclei of $\Gamma_{\rm p} = 2.75$ corresponding to $\mathcal{Q}_{0.1-100\,{\rm GeV}} = 7.8 \times 10^{-17}\,{\rm s^{-1}\,H\text{-}atom^{-1}\,cm^3}$.

A consistency check for this simple approach can be performed for the specific case of the MW, for which the column density of material traversed by CR nuclei, or "grammage," is well known (e.g., Dogiel et al. 2002). The mean escape length for CR nuclei in the MW is $\bar{x} = \tau_{\rm res}\, m_{\rm p}\, \langle n_{\rm eff}\rangle\, c \approx 12\,{\rm g\,cm^{-2}}$ (Jones et al. 2001; cf. the interaction length is $\sim$55 g cm^{-2}). We may equivalently express Equation (15) in terms of the escape length as

$$L_{0.1-100\,{\rm GeV},\pi^0} = 6.0 \times 10^{38}\,{\rm erg\,s^{-1}} \left(\frac{\rm SFR}{M_\odot\,{\rm yr^{-1}}}\right)\left(\frac{E_{\rm SN}}{10^{51}\,{\rm erg}}\right)$$
$$\times \left(\frac{\eta}{0.1}\right)\left(\frac{\bar{x}}{10\,{\rm g\,cm^{-2}}}\right). \qquad (16)$$

If we take SFR $= 1.6\,M_\odot\,{\rm yr^{-1}}$ corresponding to an SN rate of 1.9 ($\pm$1.1) per century (Diehl et al. 2006), then our estimate for the pionic gamma-ray luminosity of the MW becomes

$$L_{0.1-100\,{\rm GeV},\pi^0} = 1.1 \times 10^{39}\,{\rm erg\,s^{-1}} \left(\frac{E_{\rm SN}}{10^{51}\,{\rm erg}}\right)\left(\frac{\eta}{0.1}\right). \qquad (17)$$

For comparison, the luminosity estimated from a full numerical treatment (GALPROP code) incorporating an ensemble of multiwavelength and CR measurements is $L_{0.1-100\,{\rm GeV},\pi^0} = (5$–$7) \times 10^{38}\,{\rm erg\,s^{-1}}$, with $E_{\rm SN}\eta = (0.3$–$1) \times 10^{50}$ erg (Strong et al. 2010).

It is commonly assumed that the kinetic energy released per SN, and acceleration efficiency are universal from galaxy to galaxy. In that case, the model expressed in Equations (15) and (16) implies that the hadronic gamma-ray luminosity of the ISM scales linearly with the SFR, and with the product of residence time and effective ambient gas density (or equivalently, grammage). These quantities are likely correlated in real galaxies. For example, several authors have argued that SFRs and gas densities are related (e.g.,

via the Schmidt–Kennicutt law) so that a nonlinear scaling of gamma-ray luminosities with SFRs should be expected: $L_{0.1-100\,{\rm GeV},\pi^0} \propto {\rm SFR}^{1.4-1.7}$ (Persic & Rephaeli 2010; Fields et al. 2010).

In general, the residence time of CR nuclei in a galaxy, $\tau_{\rm res}$, can be expressed as

$$\tau_{\rm res}^{-1} = \tau_{\rm esc}^{-1} + \tau_{\rm pp}^{-1}. \qquad (18)$$

A galaxy becomes a "calorimeter" of CR nuclei when the residence time approximately equals the collisional energy loss timescale, $\tau_{\rm res} \approx \tau_{\rm pp}$, i.e., energy losses are dominated by inelastic collisions with interstellar matter rather than by escape of energetic particles. The proton–proton collisional energy loss timescale depends primarily on the average gas density encountered by CR nuclei, and is nearly independent of energy because the inelastic cross section, $\sigma_{\rm pp}$, is only weakly energy dependent for CRs with kinetic energies greater than $\sim$1 GeV. The collisional energy loss timescale is (Mannheim & Schlickeiser 1994)

$$\tau_{\rm pp} \approx (0.65 \langle n_{\rm eff}\rangle\, \sigma_{\rm pp}\, c)^{-1} \approx 5 \times 10^7\,{\rm yr} \left(\frac{\langle n_{\rm eff}\rangle}{{\rm cm^{-3}}}\right)^{-1}. \qquad (19)$$

By contrast, the escape energy loss timescale,

$$\tau_{\rm esc}^{-1} = \tau_{\rm dif}^{-1} + \tau_{\rm adv}^{-1}, \qquad (20)$$

may be energy dependent since the diffusion time, $\tau_{\rm dif}$, depends upon particle rigidity in interstellar magnetic fields. For the MW, the main contribution to the gamma-ray luminosity comes from photons with energies $\sim$1 GeV, corresponding to CR proton energies of $\sim$10 GeV. The diffusive escape timescale can be estimated as $\tau_{\rm dif} \sim z_h^2/6D \sim (1$–$2) \times 10^7$ yr for a halo height of $z_h = 4$ kpc, and taking diffusion coefficients in the range $D = (4$–$8) \times 10^{28}\,{\rm cm^2\,s^{-1}}$ for a particle rigidity of $\sim$10 GV (Ptuskin et al. 2006). Given a grammage of 12 g cm^{-3}, the average gas density corresponding to an escape time of 2×10^7 yr is $\langle n_{\rm eff}\rangle \approx 0.3$ cm^{-3} (implying that $\tau_{\rm pp} \sim 1.5 \times 10^8$ yr). In spite of modeling differences, it is generally understood that the diffusive escape timescale is much shorter than the collisional loss timescale for the MW (Strong et al. 2007, and references therein).

Large uncertainties exist for the escape time due to uncertainty in diffusion parameters, and because CRs might also be advected outward by bulk motion "superwinds" which are observed for many starbursts (Lehnert & Heckman 1996). The advective timescale, $\tau_{\rm adv}$, like the collisional energy loss timescale, is nearly independent of energy.

The spectrum of pionic gamma rays will be affected by a transition between dominant energy loss mechanisms, becoming softer for galaxies in which energy-dependent diffusive losses are important. In particular, the harder gamma-ray spectra found for starburst galaxies may be understood if the energy loss rate due to either proton–proton interactions or advection is considerably faster than the diffusion timescale. A scaling relation for gamma-ray luminosity should include the possibility that residence times for CR nuclei in different galaxies may vary substantially.

In the calorimetric limit, the residence time and effective density of target material are inversely proportional, and accordingly, the anticipated scaling of pionic gamma-ray luminosity becomes a linear scaling of the SFR:

$$L_{0.1-100\,\mathrm{GeV},\pi^0}|_{\tau_{\mathrm{res}}\approx\tau_{\mathrm{pp}}} = 5 \times 10^{39}\,\mathrm{erg\,s^{-1}} \left(\frac{\mathrm{SFR}}{M_\odot\,\mathrm{yr^{-1}}}\right)$$
$$\times \left(\frac{E_{\mathrm{SN}}}{10^{51}\,\mathrm{erg}}\right)\left(\frac{\eta}{0.1}\right). \qquad (21)$$

For the calorimeter case, we assume an underlying spectrum of CR nuclei described by a power law with $\Gamma_{\mathrm{p}} = 2.2$ ($\mathcal{Q}_{0.1-100\,\mathrm{GeV}} = 7.9 \times 10^{-17}\,\mathrm{s^{-1}\,H\text{-}atom^{-1}\,cm^3}$), representative of the LAT-detected starbursts. The gamma-ray luminosity expected in the calorimetric limit for CR nuclei is plotted in Figures 3 and 4 assuming an average CR luminosity per SN of $E_{\mathrm{SN}}\,\eta = 10^{50}$ erg.[59]

To determine how well the theoretical calorimetric limit above describes nearby starburst galaxies, we can transform the observed scaling relation between gamma-ray luminosity and total IR luminosity to a scaling relation between gamma-ray luminosity and SFR using Equation (1). This produces

$$L_{0.1-100\,\mathrm{GeV}}|_{\text{scaling relation}} = N\left(\frac{\mathrm{SFR}}{M_\odot\,\mathrm{yr^{-1}}}\,\frac{1}{1.7\epsilon}\right)^\alpha, \qquad (22)$$

where $N = 1.85^{+0.37}_{-0.31} \times 10^{39}\,\mathrm{erg\,s^{-1}}$ and $\alpha = 1.16 \pm 0.07$, fit using the EM algorithm for the complete sample of 69 galaxies. Substituting best-fit values for the normalization and index, and assuming a Chabrier IMF ($\epsilon = 0.79$) yields

$$L_{0.1-100\,\mathrm{GeV}}|_{\text{scaling relation}} \approx (1.3 \pm 0.3) \times 10^{39}\,\mathrm{erg\,s^{-1}}$$
$$\times \left(\frac{\mathrm{SFR}}{M_\odot\,\mathrm{yr^{-1}}}\right)^{1.16\pm0.07}. \qquad (23)$$

The ratio between the gamma-ray luminosity estimated via the observed scaling relation with total IR luminosity (Equation (23)) and predicted in the calorimetric limit for CR nuclei (Equation (21)) provides an estimate for the calorimetric efficiency of CR nuclei:

$$F_{\mathrm{cal}} \lesssim \frac{L_{0.1-100\,\mathrm{GeV}}|_{\text{scaling relation}}}{L_{0.1-100\,\mathrm{GeV},\pi^0}|_{\tau_{\mathrm{res}}\approx\tau_{\mathrm{pp}}}} \approx (0.3 \pm 0.1)$$
$$\times \left(\frac{\mathrm{SFR}}{M_\odot\,\mathrm{yr^{-1}}}\right)^{0.16\pm0.07}\left(\frac{E_{\mathrm{SN}}}{10^{51}\,\mathrm{erg}}\right)^{-1}\left(\frac{\eta}{0.1}\right)^{-1}. \quad (24)$$

This calorimetric efficiency estimate should be viewed as an upper limit because leptonic processes and individual sources must also contribute to the observed global gamma-ray emission of galaxies. We may infer from Equation (24) that starburst galaxies with SFR $\sim10\,M_\odot\,\mathrm{yr^{-1}}$ have maximum calorimetric efficiencies of 30%–50% whereas dwarf galaxies with SFR $\sim0.1\,M_\odot\,\mathrm{yr^{-1}}$ have lower calorimetric efficiencies of 10%–20%, when assuming an average CR luminosity per SN of $E_{\mathrm{SN}}\,\eta = 10^{50}$ erg, using a Chabrier IMF, and attributing all observed gamma rays to hadronic processes. Real galaxies are expected to exhibit some dispersion about the trend. The estimates presented here are in good agreement with the calculations of Lacki et al. (2011) for M82 and NGC 253. Our own MW is the only galaxy for which global gamma-ray luminosity can be compared to direct CR measurements, and the

---

[59] Lacki et al. (2011) calculated the ratio $L_{>1\,\mathrm{GeV}}/L_{8-1000\,\mu\mathrm{m}} = 3.1 \times 10^{-4}$ expected in the calorimetric limit for CR nuclei with $\Gamma_{\mathrm{p}} = 2.0$ and $E_{\mathrm{SN}}\eta = 10^{51}$ erg. Substituting the corresponding gamma-ray emissivity, $\mathcal{Q}_{>1\,\mathrm{GeV}} = 1.2 \times 10^{-16}\,\mathrm{s^{-1}\,H\text{-}atom^{-1}\,cm^3}$, into Equation (21) yields $L_{>1\,\mathrm{GeV}}/L_{8-1000\,\mu\mathrm{m}} = 2.5 \times 10^{-4}$, an agreement to within $\sim$20%.

CR energetics are in fair agreement with our estimates above considering that the estimated gamma-ray luminosity is below (but consistent with) the best-fit scaling relation.

Energy-independent cooling mechanisms for CR nuclei capable of preserving the injected spectral shape are preferred for the LAT-detected starburst galaxies given their relatively hard gamma-ray spectra. An enhancement of interaction efficiency is suggested by the slightly nonlinear scaling relations found in Section 4.3. However, the overall normalizations of these scaling relations imply that most starburst galaxies are not fully calorimetric for $E_{\mathrm{SN}}\,\eta = 10^{50}$ erg. Our present analysis does not tightly constrain the CR calorimetry scenario for ULIRGs. Energy-independent CR transport should also be examined as a potentially important energy loss mechanism for CR nuclei in starburst galaxies (see in this context Persic & Rephaeli 2012). Our observations suggest that a substantial fraction of CR energy escapes into intergalactic space for most galaxies since CR nuclei are expected to dominate the CR energy budget, but that some starburst systems such as M82, NGC 253, NGC 1068, and NGC 4945 have substantially higher calorimetric efficiencies relative to the MW. A detailed discussion of particular starburst galaxies as potential CR calorimeters is presented by Lacki et al. (2011).

5.2. Contribution to the Isotropic Diffuse Gamma-ray Background

Celestial gamma-ray radiation not resolved into individual sources is often treated as the sum two components: a spatially structured component originating mainly from CR interactions in the MW, and a nearly uniform all-sky component often called the IGRB. Shortly after the discovery of an isotropic component using the *OSO-3* satellite (Clark et al. 1968) and early spectral characterization with *SAS-2* (Fichtel et al. 1975), several authors proposed that multitudinous extragalactic sources too faint to be individually resolved must contribute to the observed flux (Strong et al. 1976; Lichti et al. 1978). The spectrum of the isotropic component has been subsequently measured with EGRET (Sreekumar et al. 1998; Strong et al. 2004), and most recently with the *Fermi*-LAT (Abdo et al. 2010f). Note that the intensity attributed to the isotropic diffuse component is *instrument dependent* in the sense that more sensitive instruments are capable of extracting fainter individual sources. In this work, the term IGRB will refer specifically to the most recent measurement reported by the *Fermi*-LAT Collaboration, consistent with a featureless power law of spectral index of 2.41 ± 0.05 between 0.2–100 GeV with integral intensity above 0.1 GeV of $1.03 \pm 0.17 \times 10^{-5}\,\mathrm{ph\,cm^{-2}\,s^{-1}\,sr^{-1}}$.

The origin of the IGRB flux is not fully understood, in part because the contribution from the most prominent extragalactic gamma-ray source class, namely, blazars, is well constrained by population synthesis techniques. More than one thousand sources at high Galactic latitudes, predominantly blazars, have now been discovered at GeV energies (Ackermann et al. 2011). The total intensity of these resolved sources averaged over the full sky is $0.44 \times 10^{-5}\,\mathrm{ph\,cm^{-2}\,s^{-1}\,sr^{-1}}$. Based on the empirically determined flux distribution of high-latitude sources, blazars with fluxes below the LAT detection threshold are expected to contribute less than 30% of the IGRB intensity (Abdo et al. 2010c).

Star-forming galaxies far outnumber AGNs in number density, but are more challenging to detect in high-energy gamma rays due to their comparatively modest luminosities and lack of beamed emission. Even with the improved sensitivities of

contemporary gamma-ray telescopes, a limited number of exclusively low-redshift star-forming galaxies are expected to be individually detected. Estimates for the collective intensity of unresolved galaxies consequently rely upon scaling relations between gamma-ray luminosity and galaxy properties (such as SFR and gas content), and studies of the evolving cosmological population of galaxies. Calculations by Pavlidou & Fields (2002) and Thompson et al. (2007) during the EGRET era, and by Fields et al. (2010), Makiya et al. (2011), and Stecker & Venters (2011) incorporating additional constraints from the first year of the *Fermi* mission demonstrated that star-forming galaxies could make a substantial contribution to the IGRB, comparable to that of the blazars.

Fields et al. (2010) pointed out that uncertainties in the estimated contribution can arise from a degeneracy between density and luminosity evolution of star-forming galaxies over cosmic time. In other words, a change in either the density of galaxies having a given SFR (density evolution), or a change in the SFR of individual galaxies (luminosity evolution) could account for variations in total SFR density with redshift. If the relationship between gamma-ray luminosity and SFR is nonlinear, such distinctions are important.

Stecker & Venters (2011) proposed an approach combining global gamma-ray luminosity scaling relations with multiwavelength luminosity functions which describe the abundances of individual galaxies within different luminosity classes over redshift. As an example of this approach, we now estimate the contribution of non-AGN-dominated star-forming galaxies to the IGRB using the relationship between gamma-ray luminosity (0.1–100 GeV) and total IR (8–1000 μm) luminosity identified in Section 4.3, together with an IR luminosity function provided by *Spitzer* observations of the VIMOS VLT Deep Survey and GOODS fields (Rodighiero et al. 2010).

This procedure requires an IR luminosity function for exclusively non-AGN-dominated star-forming galaxies. In obtaining luminosity functions from *Spitzer* data, Rodighiero et al. utilized a catalog of spectral templates to simultaneously determine the redshift and spectral classification of each galaxy in their data set. Objects classified as type-I AGNs were subsequently removed from the sample. Although some AGNs likely remain, the fractional contamination of IR-bight obscured AGNs is expected to be small compared to non-AGN galaxies (Ballantyne & Papovich 2007; Petric 2010), such that the final IR luminosity functions accurately represent the cosmic star formation history. The IR luminosity function for non-AGN galaxies published by Rodighiero et al. (given in the rest frame of the galaxies) is consistent with those found from other IR surveys (Sanders et al. 2003; Chapman et al. 2005; Le Floc'h et al. 2005; Huynh et al. 2007; Magnelli et al. 2009).

The collective intensity (ph cm^{-2} s^{-1} sr^{-1} GeV^{-1}) of unresolved star-forming galaxies at observed photon energy E_0 can be computed using the line-of-sight integral,

$$I(E_0) = \int_0^{z_{\max}} \int_{L_{\gamma,\min}}^{L_{\gamma,\max}} \Phi(L_\gamma, z) \frac{d^2 V}{dz d\Omega} \frac{dN}{dE}$$

$$\times (L_\gamma, E_0(1+z)) dL_\gamma dz, \qquad (25)$$

where $\Phi(L_\gamma, z) = d^2 N/(dV dL_\gamma)$ expresses the number density of galaxies per unit luminosity interval and $dN/dE(L_\gamma, E_0(1+z))$ is the differential photon flux of an individual galaxy with integral gamma-ray luminosity L_γ at redshift z. The factor $d^2 V/(dz d\Omega)$ represents the comoving volume element per unit

redshift and unit solid angle. We transform the integral over gamma-ray luminosity into an integral over IR luminosity using the scaling relation Equation (4) and fitted parameters from Table 3.

Given the limited number of star-forming galaxies detected in high-energy gamma rays, the spectral transition from quiescent to starburst galaxies has not yet been mapped in detail. Accordingly, two spectral model choices for star-forming galaxies in the gamma-ray energy band are used in our calculation. First, we adopt a power-law spectral model with photon index 2.2, characteristic of the LAT-detected starbursts. The second spectral model is based on a model of the global emission from the MW (Strong et al. 2010) scaled to the appropriate corresponding IR luminosity. These two spectral models should be viewed as bracketing the expected contribution since multiple galaxy types with different gamma-ray spectral characteristics contribute to the IGRB, e.g., dwarfs, quiescent spirals, and starbursts.

Only the redshift range $0 < z < 2.5$ is considered in this work because IR luminosity functions are not yet well constrained beyond $z \sim 2.5$. We explicitly assume that the relationship between gamma-ray and IR luminosity found for galaxies at $z \leqslant 0.05$ holds for galaxies at higher redshifts. Although we are unable to validate this assertion directly, the closely related RC–IR correlation does not show signs of evolution up to $z \sim 2$ (Ivison et al. 2010), and possibly to redshifts $z \gtrsim 4$ (Sargent et al. 2010). Those observations are indicative of a consistent relationship between star formation and CRs in galaxies over the past 10 Gyr.

We account for the attenuation of gamma rays by interactions with the extragalactic background light using the model of Franceschini et al. (2008). The contribution of resulting cascade emission to the IGRB is expected to be faint compared to the primary component (Makiya et al. 2011).

Estimates for the collective intensities of unresolved star-forming galaxies, including both quiescent galaxies and starbursts, in the energy range above 0.1 GeV are shown in Figure 7 relative to the first-year *Fermi*-LAT IGRB measurement. Shaded regions denote the range of statistical and systematic uncertainties. We use the scaling relation between gamma-ray luminosity and total IR luminosity obtained using the EM algorithm with the full sample of 69 galaxies, allowing for one standard deviation of variation in the fitted parameters, and include log-normal intrinsic scatter of gamma-ray luminosities. An additional 30% uncertainty is allocated for the normalization of the IR luminosity function. Using the methodology described above with the scaled MW spectral model, the estimated integral photon intensity of unresolved star-forming galaxies with redshifts $0 < z < 2.5$ above 0.1 GeV is $1.2^{+1.2}_{-0.6} \times 10^{-6}$ ph cm^{-2} s^{-1} sr^{-1}. If the power-law model is assumed, the estimated integral photon intensity is $0.8^{+0.7}_{-0.4} \times 10^{-6}$ ph cm^{-2} s^{-1} sr^{-1}. These estimates cover a range of 4%–23% of the integral IGRB intensity above 0.1 GeV measured with the LAT, $1.03 \pm 0.17 \times 10^{-5}$ ph cm^{-2} s^{-1} sr^{-1} (Abdo et al. 2010f). Differential intensities for the two spectral models are presented in Table 6. The range of intensities predicted in this work is consistent with previous estimates for the intensity of unresolved star-forming galaxies shown in Figure 7 for comparison.

The relative contributions of star-forming galaxies to the IGRB according to their redshift and IR luminosity class are shown in Figure 8. In both panels, fractional contributions are normalized to the estimated total intensity of star-forming galaxies with redshifts $0 < z < 2.5$. These panels provide important checks to the reliability of our total estimate given

Table 6
Collective Gamma-ray Intensity of Unresolved Star-forming Galaxies Relative to the IGRB

E (GeV)	Star-forming Galaxies		Isotropic Diffuse
	Re-scaled Milky Way Model $E^2 dN/dE$ (10^{-8} GeV cm^{-2} s^{-1} sr^{-1})	Power-Law Model, $\Gamma = 2.2$ $E^2 dN/dE$ (10^{-8} GeV cm^{-2} s^{-1} sr^{-1})	$E^2 dN/dE$ (10^{-8} GeV cm^{-2} s^{-1} sr^{-1})
0.10	4.0–15	4.9–18	150
0.16	4.9–18	4.5–16	120
0.25	5.4–20	4.1–15	100
0.40	5.4–20	3.7–14	82
0.63	4.9–18	3.4–12	68
1.00	4.2–15	3.1–11	57
1.6	3.3–12	2.8–10	47
2.5	2.5–9.0	2.6–9.4	39
4.0	1.9–6.7	2.4–8.6	32
6.3	1.4–4.9	2.1–7.8	27
10.0	1.0–3.6	1.9–7.1	22
16	0.75–2.7	1.8–6.5	18
25	0.55–2.0	1.6–5.8	15
40	0.39–1.4	1.4–5.1	12
63	0.26–0.94	1.2–4.3	10
100	0.16–0.56	0.89–3.2	8.6
160	0.082–0.28	0.59–2.0	...
250	0.036–0.12	0.34–1.1	...
400	0.022–0.078	0.19–0.63	...

Notes. Estimated intensities of unresolved star-forming galaxies using two different spectral model assumptions are compared to the IGRB spectrum measured by the LAT. The spectrum of the IGRB is consistent with a power law characterized by a photon index $\Gamma = 2.41 \pm 0.05$ with an integral photon intensity above 0.1 GeV of $(1.03 \pm 0.17) \times 10^{-5}$ ph cm^{-2} s^{-1} sr^{-1} (Abdo et al. 2010f). The entries in the rightmost column follow from this parameterization for the IGRB spectrum.

the uncertainty in the relationship between gamma-ray and IR luminosity for all galaxy types (e.g., no ULIRGs are detected at GeV energies), and our incomplete knowledge of the IR luminosity function at intermediate redshifts. The black dashed curve indicates the total IR luminosity above which Rodighiero et al. (2010) report completeness in the sample of galaxies used to derive their published IR luminosity functions. The luminosity function in the region of phase space with IR luminosity above that threshold is well constrained by *Spitzer* data. Although the IR luminosity function for galaxies below this threshold is not directly determined by the detections of individual galaxies, the total density of IR emission is constrained by the observed extragalactic background light. The IR luminosity functions presented by Rodighiero et al. (2010) integrated over IR luminosity and redshift are consistent with the cosmic SFR history estimated from analyses of IR observations by Pérez-González et al. (2005), Le Floc'h et al. (2005), and Caputi et al. (2007), and that estimated with far-ultraviolet data (Tresse et al. 2007).

Although the contribution from star-forming galaxies is only considered in the redshift range from $0 < z < 2.5$ in this work, Figure 8 makes apparent that the contribution from star-forming galaxies at redshifts $z > 1.5$ is diminishing. The particular shape of the cumulative contribution curve in the lower panel of Figure 8 is determined mainly by the IR luminosity function.

Estimates for the combined intensities of unresolved blazars and star-forming galaxies are plotted in Figure 9. The summed contribution falls short of explaining the IGRB, suggesting that important aspects of these populations are not included in current models and/or that other high-energy source classes or diffuse processes contribute a significant fraction of the observed IGRB intensity. Dermer (2007) provides an extensive discussion of possible contributions to the IGRB.

Besides the beamed emission from blazars, in which the relativistic jet direction coincides with our line of sight, the gamma-ray emission from the cores of misaligned AGNs must also constitute part of the IGRB. More than 10 such radio galaxies have now been detected in *Fermi*-LAT data at redshifts up to $z \sim 0.7$ (Abdo et al. 2010i). A relationship between the gamma ray and radio emission of LAT-detected misaligned AGNs has been used to estimate that gamma-ray-loud radio galaxies account for ~25% of the unresolved IGRB above 0.1 GeV (Inoue 2011). However, estimates for this contribution are not yet tightly constrained due to the small sample of LAT-detected objects and uncertainties regarding the scaling relation between radio and gamma-ray luminosities.

Large-scale structure formation shocks leading to the assembly of galaxy clusters represent another interesting candidate population to explain the remaining IGRB intensity (Colafrancesco & Blasi 1998). The tenuous intergalactic medium of galaxy clusters is thought to be a reservoir for CR nuclei which accumulate over cosmological timescales. Although non-thermal leptonic populations are well established by observation of Mpc-scale radio features, no galaxy cluster has been detected in the GeV energy range (e.g., Ackermann et al. 2010). Other extragalactic source classes have been considered, such as gamma-ray bursts (Le & Dermer 2007), and extended emission from the lobes of radio galaxies (Stawarz et al. 2006; Massaro & Ajello 2011), but these contributions are expected to be less than 1% in the GeV energy range. Unresolved radio-quiet AGNs are also not expected to make a significant contribution to the IGRB (Teng et al. 2011).

An example of a truly diffuse component is the cumulative emission resulting from electromagnetic cascades of ultra-high energy CRs interacting with cosmic microwave background photons (Berezinskii & Smirnov 1975) and very high energy photons interacting with the extragalactic background light (Coppi & Aharonian 1997). The gamma rays produced by those cascades are expected to have a relatively hard spectrum. Already, the LAT IGRB measurement has been used to constrain
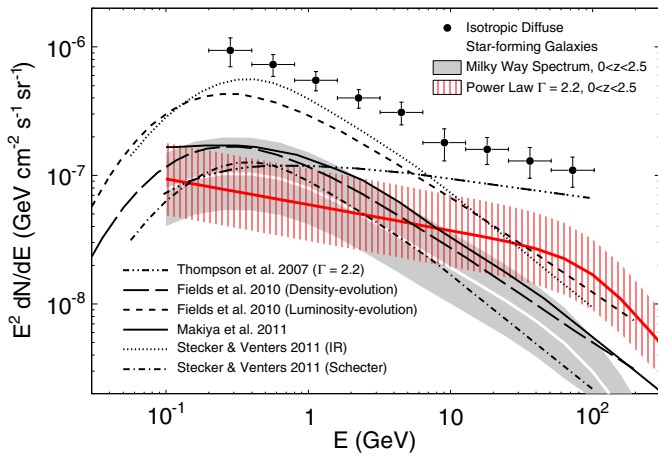
Figure 7. Estimated contribution of unresolved star-forming galaxies (both quiescent and starburst) to the isotropic diffuse gamma-ray emission measured by the *Fermi*-LAT (black points; Abdo et al. 2010f). The shaded regions indicate combined statistical and systematic uncertainties in the contributions of the respective populations. Two different spectral models are used to estimate the GeV gamma-ray emission from star-forming galaxies: a power law with photon index 2.2, and a spectral shape based on a numerical model of the global gamma-ray emission of the Milky Way (Strong et al. 2010). These two spectral models should be viewed as bracketing the expected contribution since multiple star-forming galaxy types contribute, e.g., dwarfs, quiescent spirals, and starbursts. We consider only the contribution of star-forming galaxies in the redshift range $0 < z < 2.5$. The gamma-ray opacity of the universe is treated using the extragalactic background light model of Franceschini et al. (2008). Several previous estimates for the intensity of unresolved star-forming galaxies are shown for comparison. Thompson et al. (2007) treated starburst galaxies as calorimeters of CR nuclei. The normalization of the plotted curve depends on the assumed acceleration efficiency of SNRs (0.03 in this case). The estimates of Fields et al. (2010) and by Makiya et al. (2011) incorporate results from the first year of LAT observations. Fields et al. (2010) considered the extreme cases of either pure luminosity evolution and pure density evolution of star-forming galaxies. Two recent predictions from Stecker & Venters (2011) are plotted: one assuming a scaling relation between IR-luminosity and gamma-ray luminosity, and one using a redshift-evolving Schechter model to relate galaxy gas mass to stellar mass.

(A color version of this figure is available in the online journal.)

this component and to predict the cosmogenic ultra-high energy neutrino flux originating from charged pion decays of the ultra-high energy CR interactions (Ahlers et al. 2010; Berezinsky et al. 2011; Wang et al. 2011).

Galactic sources, such as a population of unresolved millisecond pulsars at high Galactic latitudes, could become confused with isotropic diffuse emission as argued by Faucher-Giguère & Loeb (2010). Part of the IGRB may also come from our Solar System as a result of CR interactions with debris of the Oort Cloud (Moskalenko & Porter 2009).

Finally, a portion of the IGRB may originate from "new physics" processes involving, for instance, the annihilation or decay of dark matter particles (Bergström et al. 2001; Ullio et al. 2002; Taylor & Silk 2003).

Studies of anisotropies in the IGRB intensity on small angular scales provide another approach to identify IGRB constituent source populations (Siegal-Gaskins 2008). The fluctuation angular power contributed by unresolved star-forming galaxies is expected to be small compared to other source classes because star-forming galaxies have the highest spatial density among confirmed extragalactic gamma-ray emitters, but are individually faint (Ando & Pavlidou 2009). Unresolved star-forming galaxies could in principle explain the entire IGRB intensity without exceeding the measured anisotropy (Ackermann et al. 2012a). By contrast, the fractional contributions of unresolved
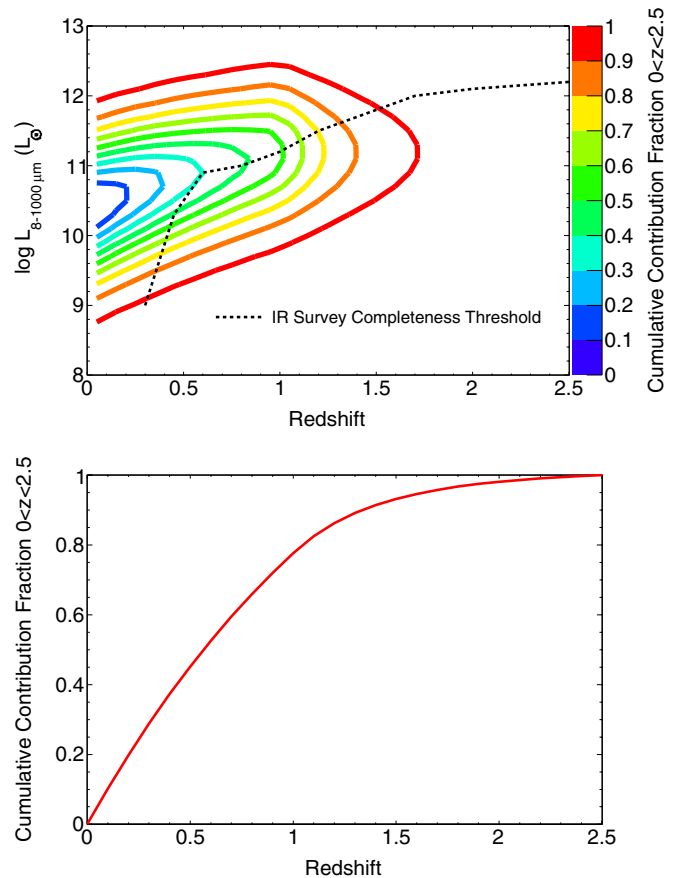
Figure 8. Relative contribution of star-forming galaxies to the isotropic diffuse gamma-ray background according to their redshift and total IR luminosity (8–1000 μm) normalized to the total contribution in the redshift range $0 < z < 2.5$. Top panel: solid contours indicate regions of phase space which contribute an increasing fraction of the total energy intensity (GeV cm^{-2} s^{-1} sr^{-1}) from all star-forming galaxies with redshifts $0 < z < 2.5$ and $10^8 L_\odot < L_{8-1000\,\mu m} < 10^{13} L_\odot$. Contour levels are placed at 10% intervals. The largest contribution comes from low-redshift Milky Way analogues ($L_{8-1000\,\mu m} \sim 10^{10} L_\odot$) and starburst galaxies comparable to M82, NGC 253, and NGC 4945. The black dashed curve indicates the IR luminosity above which the survey used to generate the adopted IR luminosity function is believed to be complete (Rodighiero et al. 2010). Bottom panel: cumulative contribution vs. redshift. As above, only the redshift range $0 < z < 2.5$ is considered.

(A color version of this figure is available in the online journal.)

blazars and millisecond pulsars to the IGRB intensity are constrained to be less than ~20% and ~2%, respectively, due to larger angular power expected for those source classes.

6. GALAXY DETECTION OUTLOOK FOR THE *FERMI*-LAT

The scaling relations obtained in Section 4.3 allow straightforward predictions for the next star-forming galaxies which could be detected by the LAT. We use the relationship between gamma-ray luminosity and total IR luminosity to select the most promising targets over a 10 year *Fermi* mission.

We begin by creating an IR flux-limited sample of galaxies from the IRAS Revised Bright Galaxies Sample (Sanders et al. 2003) by selecting all the galaxies with 60 μm flux density greater than 10 Jy (248 galaxies). Next, 0.1–100 GeV gamma-ray fluxes of the galaxies are estimated using the scaling relation between gamma-ray luminosity and total IR luminosity. Intrinsic dispersion in the scaling relation is addressed by creating a distribution of predicted gamma-ray fluxes for each
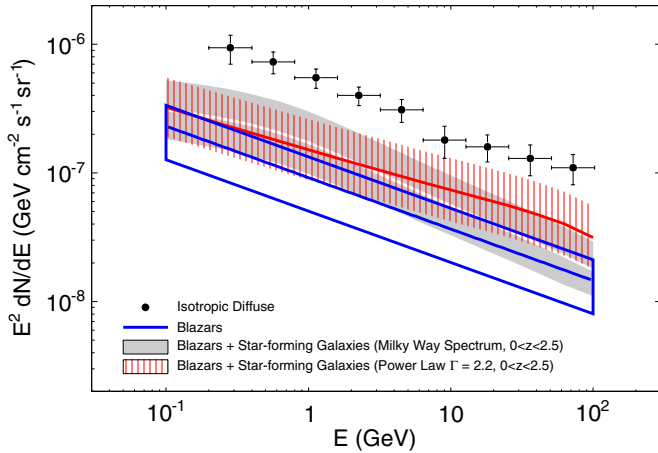
Figure 9. Same as Figure 7, but showing the summed contributions of blazars and star-forming galaxies (this work) to the isotropic diffuse gamma-ray background. Two different assumed spectral models for the star-forming galaxies are shown. The estimated contribution of blazars is derived from the distribution of observed fluxes for high Galactic latitude sources observed by the LAT, which are believed to be dominated by FSRQs and BL Lac objects (Abdo et al. 2010c).

(A color version of this figure is available in the online journal.)
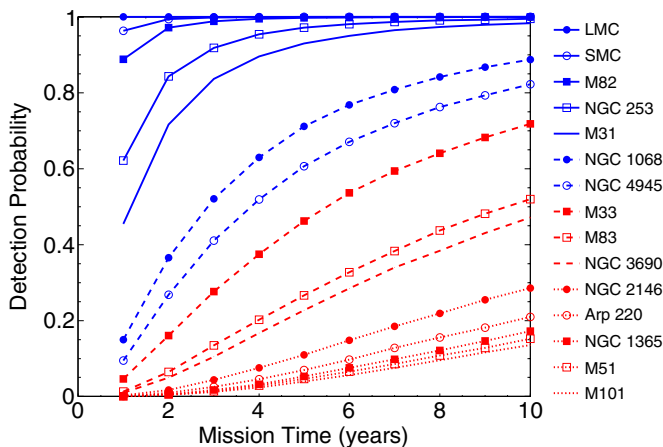
Figure 10. LAT detection probabilities for individual galaxies using the scaling relation found in Section 4.3. Galaxies already detected by the LAT are shown by blue curves, while other galaxies are drawn with red curves.

(A color version of this figure is available in the online journal.)

galaxy, assuming the log-normal intrinsic scatter fitted with the EM algorithm for the full sample of examined galaxies. Finally, we estimate the LAT flux sensitivity at the location of each galaxy given the Galactic foreground and isotropic diffuse background, and extrapolating the current LAT observation profile. For each realization of the population, we count galaxies with predicted fluxes above the LAT sensitivity thresholds at their respective positions as "detected." The galaxies are modeled as spatially unresolved sources having power-law spectral forms with photon index equal to 2.2. These modeling choices are focused on the search for additional starburst galaxies beyond the Local Group.

Detection probabilities over a 10 year *Fermi* mission are plotted in Figure 10 for the best candidate galaxies according to the procedure outlined above. The predictions pass the consistency check that the best candidate galaxies match those which have been LAT-detected. Galaxies with the next highest probabilities of LAT-detection in the coming years include M33, M83, NGC 3690, NGC 2146, and Arp 220. This list substantially
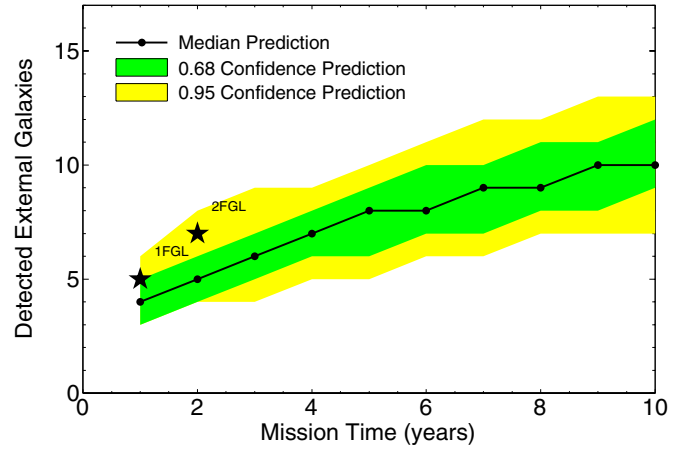
Figure 11. Total number of star-forming galaxies anticipated to be detected during a 10 year *Fermi* mission. The actual numbers of external galaxies reported in the 1FGL (Abdo et al. 2010a) and 2FGL (Nolan et al. 2012) catalogs are marked with star symbols.

(A color version of this figure is available in the online journal.)

overlaps with the top candidates recently named by Lacki et al. (2011).

Formally, the galaxy NGC 5128 (Centaurus A) would have entered our list of top candidates based on its total IR flux, and indeed, NGC 5128 has been detected at both GeV and TeV energies (Aharonian et al. 2009; Abdo et al. 2010g). However, the signal is thought to originate mainly from the relativistic jet associated with the AGN. NGC 5128 is consequently excluded from our list of candidate galaxies.

We find moderately significant excesses above backgrounds at the locations of NGC 2146 and M83 (see Section 4). If those excesses are indeed associated with the galaxies (see in this context Lenain & Walter 2011 for M83), then both might be securely detected after ~6 years of LAT observations.

Figure 11 shows the cumulative number of galaxies anticipated to be detected as a function of increasing mission time. The shaded confidence regions are obtained directly from the distribution of total galaxies above the LAT sensitivity threshold as predicted from the multiple realizations of the galaxy population described above. The actual numbers of external galaxies reported in the 1FGL (Abdo et al. 2010a) and 2FGL (Nolan et al. 2012) catalogs are consistent with expectations. If the simple scaling relationship between gamma-ray luminosity and total IR luminosity found for our present sample is representative of the larger population of low-redshift star-forming galaxies, then we can expect about 10 external galaxies to be gamma ray detected during a 10 year *Fermi* mission.

7. CONCLUSIONS

We examined 64 galaxies selected for their abundant dense molecular gas using 3 years of *Fermi*-LAT data in the 0.1–100 GeV energy range. Those results are combined with previous studies of five Local Group galaxies in a multiwavelength analysis incorporating both measured fluxes for the LAT-detected galaxies and gamma-ray flux upper limits. We find further, though not yet conclusive (*P*-values ~0.05 in the most conservative case), evidence for a quasi-linear scaling relation between gamma-ray luminosity and SFR as estimated by RC luminosity or total IR luminosity. Since contemporaneous SFRs are sensitive to short-lived massive stars, and because gamma rays are the most direct probe of CR hadrons in the ISM of

external galaxies, the scaling relationship strengthens the connection between CR energy content and massive stars which ultimately explode as SNe.

In the paradigm that SNRs channel approximately 10% of their mechanical energy into CR nuclei with kinetic energies >1 GeV, the normalization of the observed scaling relationship between gamma-ray luminosity and SFR implies that starburst galaxies (SFR $\sim 10\,M_\odot$ yr^{-1}) have an average calorimetric efficiency for CR nuclei of 30%–50% if the gamma-ray emission is dominated by neutral pion decay. As discussed in Section 5.1, this constraint depends upon the assumed energetics of SNRs and the stellar IMF. Meanwhile, the hard gamma-ray spectra of starburst galaxies ($\Gamma = 2.2$–2.3) give preference for energy-independent loss mechanisms for CR nuclei in starbursts, as opposed to the diffusive losses which likely shape the observed gamma-ray spectra of quiescent Local Group galaxies. Both hadronic interactions and advective transport of CR nuclei should be considered as potentially important energy loss mechanisms in starburst galaxies. The overall normalization of the relation between gamma-ray luminosity and SFR supports the understanding that the majority of CR energy in most galaxies eventually escapes into intergalactic space.

The relationship between gamma-ray luminosity and total IR luminosity can be used as a low-redshift anchor to estimate the contribution of star-forming galaxies to the IGRB. Using the gamma-ray luminosity scaling relations presented here in conjunction with IR luminosity functions, we estimate that star-forming galaxies with redshifts $0 < z < 2.5$ have a sky-averaged intensity of 0.4–2.4 $\times 10^{-6}$ ph cm^{-2} s^{-1} sr^{-1} in the energy range 0.1–100 GeV, thereby contributing 4%–23% of the IGRB intensity measured by the LAT. The combined contributions of unresolved blazars and star-forming galaxies appear to fall short of fully explaining the observed IGRB, suggesting that other gamma-ray source populations and/or truly diffuse processes constitute a substantial fraction of the observed IGRB intensity.

Finally, we predict that several more external galaxies might be detected by the LAT during a 10 year *Fermi* mission. In particular, the galaxies M33, M83, NGC 3690, NGC 2146, and Arp 220 are interesting targets for further study. The all-sky coverage provided by the LAT can also help identify promising targets for studies with imaging air-Cerenkov telescopes, including the proposed Cerenkov Telescope Array.[60]

APPENDIX A

KENDALL τ CORRELATION STATISTIC

The Kendall τ correlation statistic is a non-parametric rank correlation method which can be generalized for the analysis of data sets containing both detections and non-detections. In this work, we follow the procedure of Akritas & Siebert (1996) to test the degree of correlation between luminosities in two wavebands for a collection of galaxies.

Consider a data set consisting of n points, $X_k[i]$, indexed by $i = 1, \ldots, n$, with $k = 1, 2$ to denote the two wavebands. To compute the correlation coefficient, first define a helper function,

$$
\begin{aligned}
J_k(i, j) = \delta(X_k[i])I(X_k[i] < X_k[j]) \\
- \delta(X_k[j])I(X_k[j] < X_k[i])),
\end{aligned}
\tag{A1}
$$

where $I = 1$ if the enclosed conditional statement is true, and $I = 0$ otherwise. When performing an analysis of partially censored data, let $\delta(X_k[i]) = 1$ for a detection (measured value), and $\delta(X_k[i]) = 0$ for a non-detection (limiting value). For historical reasons, the Kendall τ statistic is conventionally defined in the context of data containing lower limits rather than upper limits as is common in astrophysics research applications. The method can be applied to data containing upper limits by taking the negative value of all quantities, i.e., $X'_k[i] = -X_k[i]$. Next, define a function to encode the ordering between two points in the data set labeled i, j,

$$
H(i, j) = J_1(i, j)J_2(i, j).
\tag{A2}
$$

A graphical representation of this encoding is shown in Figure 12 for a data set containing upper limits in the $k = 2$ waveband. Note that $H(i, j) \in -1, 0, 1$. The Kendall τ correlation coefficient is the sum of $H(i, j)$ for each pair of points in the data set, normalized by the total number of pairs,
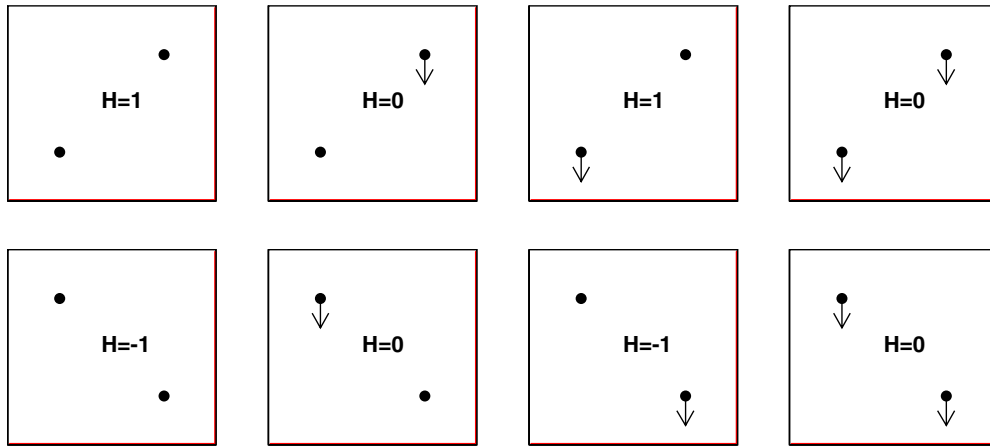
$$
\tau = \frac{2}{n(n-1)} \sum_i^n \sum_{j>i}^n H(i, j).
\tag{A3}
$$

APPENDIX B

POTENTIAL HAZARD OF MULTIWAVELENGTH COMPARISONS IN FLUX SPACE

Consider the simple case of a sample of objects observed in two wavebands, denoted by $k = 1, 2$, which follow a power-law relation in intrinsic luminosity, $\log L_2 = \alpha \log L_1 + \beta$. An

---

Figure 12. Graphical representation of the generalized Kendall τ rank correlation test. The τ correlation statistic is proportional to the sum of H-values obtained for each pair of points in the data set. See Appendix A for a complete description of the method.

(A color version of this figure is available in the online journal.)

algebraic conversion of this equation from luminosity space to flux space yields

$$\log F_2 = \alpha \log F_1 + 2(\alpha - 1) \log d + \text{constant}, \quad \text{(B1)}$$

where d is the distance to the distance to each object in the sample, $L_k = 4\pi d^2 F_k$. Note that if the relationship between intrinsic luminosities is nonlinear, $\alpha \neq 1$, the distance to each galaxy enters as an additional term in the flux space relation. This situation can lead to unpredictable behavior, since the objects in the sample are, in general, located at different distances to the observer.

APPENDIX C

SIMULATIONS OF MULTIWAVELENGTH COMPARISONS IN LUMINOSITY SPACE

We discuss results from a Monte Carlo study of multiwavelength comparisons in luminosity space in the context of the present work. One concern of comparing luminosities is that both quantities have a shared dependence on the measured distances to the objects. Common selection effects in observational astrophysics, e.g., that more luminous objects can be detected at greater distances, therefore have the potential to induce spurious apparent luminosity correlations between wavebands.

We performed a series of simulations of a population of objects observed in two wavebands to investigate this potential source of bias. The two wavebands are differentiated in that the "selection" band, here called the "X band," is used to select a sample of objects from a larger population, and the objects are then observed in a second "search" band, here called the "Y band." The bands are asymmetric in that partial censoring is possible in the Y band, whereas all objects are detected in the X band. The galaxies examined in this work fit the above description as a flux-limited sample selected according to their IR, CO-line, and HCN-line fluxes, and subsequently observed in the gamma-ray band.

We test various scenarios considering different intrinsic relationships between X- and Y-band luminosities, sample selection approaches, and detection efficiencies. Throughout the simulations, we assume that distances to the objects and fluxes are measured without error. This assumption implies completeness down to the detection threshold flux level in the Y band.

For each scenario, repeat the following procedure many times.

1. Create a population of objects with randomly distributed distances from the observer and luminosities in the X band.
2. Assume a relationship between intrinsic luminosities in the X and Y bands, specifically a power-law form with intrinsic dispersion $\mathcal{D}$:

$$\log L_Y = \alpha \log L_X + \beta + \mathcal{D}. \quad \text{(C1)}$$

Intrinsic dispersion in the relationship between luminosities in the X and Y bands is taken to be normally distributed in log space with standard deviation $\sigma_{\mathcal{D}}$, i.e., $\mathcal{D} = \mathcal{N}(0, \sigma_{\mathcal{D}})$.

3. Select a subset of objects from the full population. The subset will comprise the sample of objects observed in both wavebands and considered in subsequent statistical analysis.
4. Objects are considered detected (non-detected) in the Y band if their Y-band flux is above (below) the Y-band detection threshold flux level. For the objects which are not detected in the Y band, set the flux upper limit at the Y-band detection threshold flux level. Determine corresponding luminosities (possibly limits) for each object in the sample.
5. Compute the Kendall τ correlation coefficient for the relationship between luminosities in the X and Y bands for the subset of selected objects.

For the particular examples which follow, we generate a population of objects representative of low-redshift star-forming galaxies. The X-band luminosity distribution is drawn from the total IR luminosity function of Rodighiero et al. (2010) at redshift $z = 0$, with a minimum IR luminosity of $10^8 L_\odot$. The volume considered is a cube of 200 Mpc on a side. Objects are assumed to be uniformly distributed in Euclidean three-dimensional space.

We consider two sample selection approaches: volume-limited and flux-limited in the X band. In either case, a sample consisting of 100 objects is selected for each trial. The selected sample in each trial amounts to approximately 0.06% of objects in the full simulated population.

The parameters of each simulation scenario include the intrinsic power-law scaling index between X- and Y-band luminosities (α), the standard deviation of the intrinsic dispersion in the luminosity–luminosity relationship (σ, dex), and the detection efficiency of sample objects in the Y band. For each scenario,

Table 7
Kendall τ Correlation Coefficient Distributions: Volume-limited Sample

	$\alpha_{\rm intrinsic} = 0$	$\alpha_{\rm intrinsic} = 1$
	Detection efficiency in Y band = 0.1	
$\sigma_{\mathcal{D}} = 0$	0 ± 0	0.12 ± 0.023
	(...)	(5.1)
$\sigma_{\mathcal{D}} = 0.3$	-0.00021 ± 0.012	0.11 ± 0.022
	(−0.017)	(5.3)
$\sigma_{\mathcal{D}} = 1$	-0.002 ± 0.028	0.092 ± 0.024
	(−0.07)	(3.9)
	Detection efficiency in Y band = 1	
$\sigma_{\mathcal{D}} = 0$	0 ± 0	1 ± 0
	(...)	(...)
$\sigma_{\mathcal{D}} = 0.3$	-0.0018 ± 0.067	0.71 ± 0.03
	(−0.026)	(24)
$\sigma_{\mathcal{D}} = 1$	-0.0023 ± 0.068	0.36 ± 0.058
	(−0.035)	(6.2)

Notes. Mean Kendall τ correlation coefficient and standard deviation of the distribution are supplied for each set of simulation parameters: detection efficiency in the Y band, true power-law scaling index of intrinsic luminosities (α), and standard deviation of intrinsic dispersion in the luminosity–luminosity relationship ($\sigma_{\mathcal{D}}$, dex). One thousand realizations were analyzed for each set of simulation parameters. Below the mean and standard deviation of the distribution of correlation coefficients, and indicated in parentheses, is the ratio of the mean to the standard deviation.

Table 8
Kendall τ Correlation Coefficient Distributions: Flux-limited Sample

	$\alpha_{\rm intrinsic} = 0$	$\alpha_{\rm intrinsic} = 1$
	Detection efficiency in Y band = 0.1	
$\sigma_{\mathcal{D}} = 0$	0 ± 0	0.068 ± 0.017
	(...)	(4.1)
$\sigma_{\mathcal{D}} = 0.3$	0.00074 ± 0.0056	0.072 ± 0.018
	(0.13)	(4.1)
$\sigma_{\mathcal{D}} = 1$	0.0027 ± 0.017	0.065 ± 0.021
	(0.16)	(3.1)
	Detection efficiency in Y band = 1	
$\sigma_{\mathcal{D}} = 0$	0 ± 0	1 ± 0
	(...)	(...)
$\sigma_{\mathcal{D}} = 0.3$	0.00004 ± 0.067	0.73 ± 0.03
	(0.00055)	(24)
$\sigma_{\mathcal{D}} = 1$	0.0018 ± 0.07	0.38 ± 0.057
	(0.025)	(6.6)

Note. Same as Table 7, but considering flux-limited samples of objects in X-band flux.

we perform 1000 trials. The distributions of Kendall τ correlation coefficients for the different scenarios are summarized in Table 7 for the case of volume-limited sample selection, and in Table 8 for the case of flux-limited sample selection.

Volume-limited samples are generally considered to be unbiased, provided that a large enough volume can be sensitively probed so as to contain a distribution of objects representative of the full population. The results contained in Table 7 demonstrate that in scenarios with no intrinsic relationship between luminosities ($\alpha = 0$), the distribution of correlation coefficients is consistent with being centered on zero ($\tau = 0$ corresponds to no correlation). The correlation test is not biased toward finding a non-existent correlation in this example. By contrast, the distribution of correlation coefficients for scenarios in which an intrinsic linear correlation was considered ($\alpha = 1$) consis-

tently tend toward positive values, thereby correctly identifying a positive correlation.

These conclusions do not change appreciably in flux-limited sample selection case, as evident in Table 8. For the simple examples above, which are modeled on the population of star-forming galaxies examined in this work in terms of luminosity distribution, sample size, and sample selection, the Kendall τ correlation coefficient proves to be effective in distinguishing between populations with and without intrinsically correlated luminosities, even when only a small fraction of objects are actually detected in the "search" band.

We considered the simple case of power-law relation between intrinsic luminosities for this study. However, since the Kendall τ correlation test is a non-parametric method, the conclusions are expected to hold for more complex scaling relations as well.

REFERENCES

Abdo, A. A., Ackermann, M., Ajello, M., et al. 2009a, Astropart. Phys., 32, 193
Abdo, A. A., Ackermann, M., Ajello, M., et al. 2009b, Phys. Rev. D, 80, 122004
Abdo, A. A., Ackermann, M., Ajello, M., et al. 2010a, ApJS, 188, 405
Abdo, A. A., Ackermann, M., Ajello, M., et al. 2010b, A&A, 523, L2
Abdo, A. A., Ackermann, M., Ajello, M., et al. 2010c, ApJ, 720, 435
Abdo, A. A., Ackermann, M., Ajello, M., et al. 2010d, ApJ, 709, L152
Abdo, A. A., Ackermann, M., Ajello, M., et al. 2010e, A&A, 512, A7
Abdo, A. A., Ackermann, M., Ajello, M., et al. 2010f, Phys. Rev. Lett., 104, 101101
Abdo, A. A., Ackermann, M., Ajello, M., et al. 2010g, ApJ, 719, 1433
Abdo, A. A., Ackermann, M., Ajello, M., et al. 2010h, A&A, 523, A46
Abdo, A. A., Ackermann, M., Ajello, M., et al. 2010i, ApJ, 720, 912
Acciari, V. A., Aliu, E., Arlen, T., et al. 2009, Nature, 462, 770
Acero, F., Aharonian, F., Akhperjanian, A. G., et al. 2009, Science, 326, 1080
Ackermann, M., Ajello, M., Albert, A., et al. 2012a, Phys. Rev. D, 85, 083007
Ackermann, M., Ajello, M., Allafort, A., et al. 2010, ApJ, 717, L71
Ackermann, M., Ajello, M., Allafort, A., et al. 2011, ApJ, 743, 171
Ackermann, M., Ajello, M., Allafort, A., et al. 2012b, ApJ, 747, 104
Adriani, O., Barbarino, G. C., Bazilevskaya, G. A., et al. 2011, Science, 332, 69
Aharonian, F., Akhperjanian, A. G., Anton, G., et al. 2009, ApJ, 695, L40
Aharonian, F., Akhperjanian, A. G., Bazer-Bachi, A. R., et al. 2005, A&A, 441, 465
Ahlers, M., Anchordoqui, L. A., Gonzalez-Garcia, M. C., Halzen, F., & Sarkar, S. 2010, Astropart. Phys., 34, 106
Akritas, M. G., & Siebert, J. 1996, MNRAS, 278, 919
Akyüz, A., Brouillet, N., & Özel, M. E. 1991, A&A, 248, 419
Albert, J., Aliu, E., Anderhub, H., et al. 2007, ApJ, 658, 245
Ando, S., & Pavlidou, V. 2009, MNRAS, 400, 2122
Appleton, P. N., Fadda, D. T., Marleau, F. R., et al. 2004, ApJS, 154, 147
Atwood, W. B., Abdo, A. A., Ackermann, M., et al. 2009, ApJ, 697, 1071
Ballantyne, D. R., & Papovich, C. 2007, ApJ, 660, 988
Baumgartner, W. H., Tueller, J., Markwardt, C., & Skinner, G. 2010, BAAS, 42, 675
Berezinsky, V., Gazizov, A., Kachelrieß, M., & Ostapchenko, S. 2011, Phys. Lett. B, 695, 13
Berezinskii, V. S., & Smirnov, A. I. 1975, Ap&SS, 32, 461
Bergström, L., Edsjö, J., & Ullio, P. 2001, Phys. Rev. Lett., 87, 251301
Bertsch, D. L., Dame, T. M., Fichtel, C. E., et al. 1993, ApJ, 416, 587
Bloemen, J. B. G. M. 1985, A&A, 145, 391
Blom, J. J., Paglione, T. A. D., & Carramiñana, A. 1999, ApJ, 516, 744
Burlon, D., Ajello, M., Greiner, J., et al. 2011, ApJ, 728, 58
Caputi, K. I., Lagache, G., Yan, L., et al. 2007, ApJ, 660, 97
Chabrier, G. 2003, PASP, 115, 763
Chapman, S. C., Blain, A. W., Smail, I., & Ivison, R. J. 2005, ApJ, 622, 772
Cillis, A. N., Torres, D. F., & Reimer, O. 2005, ApJ, 621, 139
Clark, G. W., Garmire, G. P., & Kraushaar, W. L. 1968, ApJ, 153, L203
Colafrancesco, S., & Blasi, P. 1998, Astropart. Phys., 9, 227
Condon, J. J. 1992, ARA&A, 30, 575
Condon, J. J., Anderson, M. L., & Helou, G. 1991, ApJ, 376, 95
Condon, J. J., Cotton, W. D., Greisen, E. W., et al. 1998, AJ, 115, 1693
Condon, J. J., Helou, G., Sanders, D. B., & Soifer, B. T. 1990, ApJS, 73, 359
Coppi, P. S., & Aharonian, F. A. 1997, ApJ, 487, L9
Crain, R. A., McCarthy, I. G., Frenk, C. S., Theuns, T., & Schaye, J. 2010, MNRAS, 407, 1403
de Cea del Pozo, E., Torres, D. F., & Rodriguez Marrero, A. Y. 2009, ApJ, 698, 1054

de Jong, T., Klein, U., Wielebinski, R., & Wunderlich, E. 1985, A&A, 147, L6
Dennison, B., Balonek, T. J., Terzian, Y., & Balick, B. 1975, PASP, 87, 83
Dermer, C. D. 2007, in AIP Conf. Proc. 921, The First GLAST Symposium, ed. S. Ritz, P. Michelson, & C. A. Meegan (Melville, NY: AIP), 122
Diehl, R., Halloin, H., Kretschmer, K., et al. 2006, Nature, 439, 45
Dogiel, V. A., Schönfelder, V., & Strong, A. W. 2002, ApJ, 572, L157
Domingo-Santamaría, E., & Torres, D. F. 2005, A&A, 444, 403
Dressel, L. L. 1988, ApJ, 329, L69
Drury, L. O., Aharonian, F. A., & Voelk, H. J. 1994, A&A, 287, 959
Efron, B., & Petrosian, V. 1999, J. Am. Stat. Assoc., 94, 824
Faucher-Giguère, C.-A., & Loeb, A. 2010, J. Cosmol. Astropart. Phys., JCAP01(2010)005
Feigelson, E. D., & Berg, C. J. 1983, ApJ, 269, 400
Fichtel, C. E., Hartman, R. C., Kniffen, D. A., et al. 1975, ApJ, 198, 163
Fields, B. D., Pavlidou, V., & Prodanović, T. 2010, ApJ, 722, L199
Franceschini, A., Rodighiero, G., & Vaccari, M. 2008, A&A, 487, 837
Freedman, W. L., Madore, B. F., Gibson, B. K., et al. 2001, ApJ, 553, 47
Gao, Y., & Solomon, P. M. 2004a, ApJS, 152, 63
Gao, Y., & Solomon, P. M. 2004b, ApJ, 606, 271
Ginzburg, V. L., & Syrovatskii, S. I. (ed.) 1964, The Origin of Cosmic Rays (New York: Macmillan)
Helou, G., Soifer, B. T., & Rowan-Robinson, M. 1985, ApJ, 298, L7
Hughes, A., Staveley-Smith, L., Kim, S., Wolleben, M., & Filipović, M. 2007, MNRAS, 382, 543
Huynh, M. T., Frayer, D. T., Mobasher, B., et al. 2007, ApJ, 667, L9
Inoue, Y. 2011, ApJ, 733, 66
Isobe, T., Feigelson, E. D., & Nelson, P. I. 1986, ApJ, 306, 490
Ivison, R. J., Magnelli, B., Ibar, E., et al. 2010, A&A, 518, L31
Jones, F. C., Lukasiak, A., Ptuskin, V., & Webber, W. 2001, ApJ, 547, 264
Kamae, T., Karlsson, N., Mizuno, T., Abe, T., & Koi, T. 2006, ApJ, 647, 692
Kembhavi, A., Feigelson, E. D., & Singh, K. P. 1986, MNRAS, 220, 51
Kennicutt, R. C., Jr. 1998a, ARA&A, 36, 189
Kennicutt, R. C., Jr. 1998b, ApJ, 498, 541
Lacki, B. C., Thompson, T. A., & Quataert, E. 2010, ApJ, 717, 1
Lacki, B. C., Thompson, T. A., Quataert, E., Loeb, A., & Waxman, E. 2011, ApJ, 734, 107
Lande, J., Ackermann, M., Allafort, A., et al. 2012, ApJ, 756, 5
LaValley, M., Isobe, T., & Feigelson, E. 1992, in ASP Conf. Ser. 25, Astronomical Data Analysis Software and Systems I, ed. D. M. Worrall, C. Biemesderfer, & J. Barnes (San Francisco, CA: ASP), 245
Le, T., & Dermer, C. D. 2007, in AIP Conf. Proc. 921, The First GLAST Symposium, ed. S. Ritz, P. Michelson, & C. A. Meegan (Melville, NY: AIP), 462
Le Floc'h, E., Papovich, C., Dole, H., et al. 2005, ApJ, 632, 169
Lehnert, M. D., & Heckman, T. M. 1996, ApJ, 462, 651
Lenain, J.-P., Ricci, C., Türler, M., Dorner, D., & Walter, R. 2010, A&A, 524, A72
Lenain, J.-P., & Walter, R. 2011, A&A, 535, A19
Lichti, G. G., Bignami, G. F., & Paul, J. A. 1978, Ap&SS, 56, 403
Liu, F., & Gao, Y. 2010, ApJ, 713, 524
Loiseau, N., Klein, U., Greybe, A., Wielebinski, R., & Haynes, R. F. 1987, A&A, 178, 62
Magnelli, B., Elbaz, D., Chary, R. R., et al. 2009, A&A, 496, 57
Makiya, R., Totani, T., & Kobayashi, M. A. R. 2011, ApJ, 728, 158
Mannheim, K., & Schlickeiser, R. 1994, A&A, 286, 983
Marsh, K. A., & Helou, G. 1995, ApJ, 445, 599
Massaro, F., & Ajello, M. 2011, ApJ, 729, L12
Mattox, J. R., Bertsch, D. L., Chiang, J., et al. 1996, ApJ, 461, 396
Mori, M. 2009, Astropart. Phys., 31, 341
Moskalenko, I. V., & Porter, T. A. 2009, ApJ, 692, L54
Murphy, E. J., Braun, R., Helou, G., et al. 2006, ApJ, 638, 157
Nolan, P. L., Abdo, A. A., Ackermann, M., et al. 2012, ApJS, 199, 31

Ohm, S., De Naurois, M., Voelk, H., et al. 2011, Presentation at 32nd International Cosmic Ray Conference, Beijing, abstract available at http://galprop.stanford.edu/elibrary/icrc/2011/papers/OG2.3/icrc0270.pdf
Paglione, T. A. D., Marscher, A. P., Jackson, J. M., & Bertsch, D. L. 1996, ApJ, 460, 295
Paladino, R., Murgia, M., Helfer, T. T., et al. 2006, A&A, 456, 847
Pavlidou, V., & Fields, B. D. 2002, ApJ, 575, L5
Pérez-González, P. G., Rieke, G. H., Egami, E., et al. 2005, ApJ, 630, 82
Persic, M., & Rephaeli, Y. 2010, MNRAS, 403, 1569
Persic, M., & Rephaeli, Y. 2012, arXiv:1201.0369
Persic, M., Rephaeli, Y., & Arieli, Y. 2008, A&A, 486, 143
Petric, A. 2010, in AIP Conf. Proc. 1240, Hunting for the Dark: The Hidden Side of Galaxy Formation, ed. V. P. Debattista & C. C. Popescu (Melville, NY: AIP), 76
Ptuskin, V. S., Moskalenko, I. V., Jones, F. C., Strong, A. W., & Zirakashvili, V. N. 2006, ApJ, 642, 902
Rephaeli, Y., Arieli, Y., & Persic, M. 2010, MNRAS, 401, 473
Rodighiero, G., Vaccari, M., Franceschini, A., et al. 2010, A&A, 515, A8
Salpeter, E. E. 1955, ApJ, 121, 161
Sanders, D. B., Mazzarella, J. M., Kim, D.-C., Surace, J. A., & Soifer, B. T. 2003, AJ, 126, 1607
Sanders, D. B., & Mirabel, I. F. 1996, ARA&A, 34, 749
Sanuki, T., Motoki, M., Matsumoto, H., et al. 2000, ApJ, 545, 1135
Sargent, M. T., Schinnerer, E., Murphy, E., et al. 2010, ApJ, 714, L190
Scoville, N., & Young, J. S. 1983, ApJ, 265, 148
Siegal-Gaskins, J. M. 2008, J. Cosmol. Astropart. Phys., JCAP10(2008)040
Simpson, J. A. 1983, Annu. Rev. Nucl. Part. Sci., 33, 323
Solomon, P. M., Downes, D., & Radford, S. J. E. 1992, ApJ, 387, L55
Solomon, P. M., Sanders, D. B., & Scoville, N. Z. 1979, in IAU Symp. 84, The Large-scale Characteristics of the Galaxy, ed. W. B. Burton (Cambridge: Cambridge Univ. Press), 35
Sreekumar, P., Bertsch, D. L., Dingus, B. L., et al. 1998, ApJ, 494, 523
Stawarz, Ł., Kneiske, T. M., & Kataoka, J. 2006, ApJ, 637, 693
Stecker, F. W. 2007, Astropart. Phys., 26, 398
Stecker, F. W., & Venters, T. M. 2011, ApJ, 736, 40
Strong, A. W. 2007, Ap&SS, 309, 35
Strong, A. W., Moskalenko, I. V., & Ptuskin, V. S. 2007, Annu. Rev. Nucl. Part. Sci., 57, 285
Strong, A. W., Moskalenko, I. V., & Reimer, O. 2004, ApJ, 613, 956
Strong, A. W., Porter, T. A., Digel, S. W., et al. 2010, ApJ, 722, L58
Strong, A. W., Wolfendale, A. W., & Worrall, D. M. 1976, MNRAS, 175, 23P
Taylor, J. E., & Silk, J. 2003, MNRAS, 339, 505
Teng, S. H., Mushotzky, R. F., Sambruna, R. M., Davis, D. S., & Reynolds, C. S. 2011, ApJ, 742, 66
Thompson, T. A., Quataert, E., & Waxman, E. 2007, ApJ, 654, 219
Thompson, T. A., Quataert, E., Waxman, E., Murray, N., & Martin, C. L. 2006, ApJ, 645, 186
Torres, D. F. 2004, ApJ, 617, 966
Torres, D. F., Reimer, O., Domingo-Santamaría, E., & Digel, S. W. 2004, ApJ, 607, L99
Tresse, L., Ilbert, O., Zucca, E., et al. 2007, A&A, 472, 403
Ullio, P., Bergström, L., Edsjö, J., & Lacey, C. 2002, Phys. Rev. D, 66, 123502
van der Kruit, P. C. 1971, A&A, 15, 110
van der Kruit, P. C. 1973, A&A, 29, 263
Völk, H. J. 1989, A&A, 218, 67
Wang, X.-Y., Liu, R.-Y., & Aharonian, F. 2011, ApJ, 736, 112
Woosley, S. E., & Weaver, T. A. 1995, ApJS, 101, 181
Wright, A., & Otrupcek, R. 1990, PKS Catalog, 0
Wrobel, J. M., & Heeschen, D. S. 1988, ApJ, 335, 677
Wrobel, J. M., & Heeschen, D. S. 1991, AJ, 101, 148
Wu, J., Evans, N. J., II, Gao, Y., et al. 2005, ApJ, 635, L173
Wunderlich, E., Wielebinski, R., & Klein, U. 1987, A&AS, 69, 487
Yun, M. S., Reddy, N. A., & Condon, J. J. 2001, ApJ, 554, 803